Department of Radio Science and Engineering

Uncertainty in computational RF dosimetry

Ilkka Laakso

Aalto University

Uncertainty in computational RF dosimetry

Ilkka Laakso

Doctoral dissertation for the degree of Doctor of Science in Technology to be presented with due permission of the School of Electrical Engineering for public examination and debate in Auditorium S1 at the Aalto University School of Electrical Engineering (Espoo, Finland) on the 4th of February 2011 at 12 noon.

Supervisor
Professor Keijo Nikoskinen

Instructor
Professor Keijo Nikoskinen

Preliminary examiners
Dr Kimmo Kärkkäinen
Dr Jafar Keshvari

Opponent
Associate Professor Akimasa Hirata

Author
Ilkka Laakso

Abstract

Radio-frequency (RF) electromagnetic field dosimetry studies the absorption of electromagnetic energy inside the human body. The absorbed energy is measured in terms of the specific absorption rate (SAR), which is linked to the possible adverse thermal effects of the exposure to RF electromagnetic fields. With advances in computational power and accurate numerical models of the human anatomy, computational methods have gained an increasingly significant role in RF dosimetry in recent years. Nowadays, the finite-difference time-domain (FDTD) method is the most widely used numerical technique in computational RF dosimetry.

Computational analysis of the SAR features many modelling and approximation phases that may introduce error and uncertainty. The emphasis of this thesis is to study how reliably the SAR can be assessed by the FDTD method, and how various modelling choices affect the accuracy of the simulated results. In addition to the SAR, also the temperature rise due to the electromagnetic power absorption and its modelling by the bioheat equation is studied.

The results of the thesis help to evaluate and identify the possible uncertainty factors and sources of error in computational RF dosimetry, which will produce new information on the reliability and repeatability of computational exposure assessment. Studying the uncertainty and accuracy of the methods also allows, for example, lessening the computational requirements and improving the accuracy of the simulations.

Tiivistelmäteksti

Radiotaajuisten (RF) sähkömagneettisten kenttien dosimetria tutkii sähkömagneettisen energian absorboitumista ihmiskehon sisällä. Absorboituneen energian mittana on ominais-absorptionopeus (SAR), joka liittyy mahdollisiin sähkömagneettisille kentille altistumisen haitallisiin lämpövaikutuksiin. Laskennallisten menetelmien rooli RF dosimetriassa on kasvanut tietokoneiden ja ihmiskehon tarkkojen numeeristen mallien kehityksen myötä. Tätä nykyä aika-alueen differenssimenetelmä (FDTD) on suosituin menetelmä laskennallisessa dosimetriassa.

SAR-arvojen laskennallinen analyysi sisältää useita mallintamisvalintoja ja approksimaatioita, jotka saattavat aiheuttaa virheitä ja epävarmuuksia. Tämän työn tavoitteena on tutkia kuinka luotettavasti SAR-arvoja saadaan arvioitua FDTD-menetelmällä, ja mitkä tekijät ja mallintamisvalinnat vaikuttavat simulointitulosten tarkkuuteen. SAR-arvojen lisäksi tutkitaan myös sähkömagneettisen tehoabsorption aiheuttamaa lämpötilan nousua ja sen mallintamista biolämpöyhtälön avulla.

Työn tulokset auttavat arvioimaan ja tunnistamaan laskennallisen RF dosimetrian mahdollisia epävarmuustekijöitä ja virhettä, mikä tuottaa uutta tietoa laskennallisen altistumisen arvioinnin luotettavuudesta ja toistettavuudesta. Lisäksi menetelmien epävarmuuden ja tarkkuuden tutkiminen mahdollistaa mm. tarvittavien laskentaresurssien määrän pienentämisen sekä simulaatioiden tarkkuuden parantamisen.

Preface

This thesis was carried out in the Department of Radio Science and Engineering at Aalto University.

Otaniemi, December 2010

Ilkka Laakso

Contents

List of publications

This thesis consists of an overview and of the following publications which are referred to in the text by their Roman numerals.

(I) Ilkka Laakso, Sami Ilvonen and Tero Uusitupa, "Performance of convolutional PML absorbing boundary conditions in finite-difference time-domain SAR calculations", *Physics in Medicine and Biology*, Vol. 52, pp. 7183–7192, 2007.

(II) Ilkka Laakso and Tero Uusitupa, "Alternative approach for modeling material interfaces in FDTD", *Microwave and Optical Technology Letters*, Vol. 50, No. 5, pp. 1211–1214, 2008.

(III) T Uusitupa, S Ilvonen, I Laakso, and K Nikoskinen, "The effect of finite-difference time-domain resolution and power-loss computation method on SAR values in plane-wave exposure of Zubal phantom", *Physics in Medicine and Biology*, Vol. 53, pp. 445–452, 2008.

(IV) Ilkka Laakso, "Assessment of computational uncertainty of temperature rise and SAR in the eyes and brain under far-field exposure from 1 to 10 GHz", *Physics in Medicine and Biology*, Vol. 54, pp. 3393–3404, 2009.

(V) T Uusitupa, I Laakso, S Ilvonen, and K Nikoskinen, "SAR variation study from 300 to 5000 MHz for 15 voxel models including different postures", *Physics in Medicine and Biology*, Vol. 55, pp. 1157–1176, 2010.

(VI) Ilkka Laakso, Tero Uusitupa and Sami Ilvonen, "Comparison of SAR calculation algorithms for finite-difference time-domain method", *Physics in Medicine and Biology*, Vol. 55, pp. N421–431, 2010.

(VII) Sami Ilvonen and Ilkka Laakso, "Computational estimation of magnetically induced electric fields in a rotating head", *Physics in Medicine and Biology*, Vol. 54, pp. 341–351, 2009.

Author's contribution

(I) The author wrote the manuscript and derived most of the results. Dr Ilvonen helped in preparing the computational codes and calculated some of the results, and Dr Uusitupa calculated some of the results.

(II) The author derived the results and wrote the manuscript. The idea of the paper was based on discussions with Dr Uusitupa.

(III) Dr Uusitupa had the main responsibility for preparing the article. This author participated by writing some of the computational codes and by discussing the ideas.

(IV) This paper presents independent research of the author.

(V) Dr Uusitupa was the primary author in this paper. This author wrote some of the computational codes and assisted in preparing the manuscript.

(VI) The author derived the results and wrote the manuscript. Dr Uusitupa and Dr Ilvonen helped to improve the manuscript by their comments.

(VII) This paper was written in a close co-operation between Dr Ilvonen and this author. Both authors participated in preparing the manuscript and deriving the results.

List of abbreviations

ABC   absorbing boundary condition
CAD   computer-aided design
CFS-PML   complex frequency shifted perfectly matched layer
CPML   convolutional perfectly matched layer
CT   computed tomography
DIVA   discrete vascularized thermal diffusion model
EM   electromagnetic
EMF   electromagnetic field
FDTD   finite-difference time-domain
FEM   finite-element method
ICNIRP   International Commission on Non-Ionizing Radiation Protection
IEEE   Institute of Electrical and Electronics Engineers
MR   (nuclear) magnetic resonance
MRI   magnetic resonance imaging
PML   perfectly matched layer (absorbing boundary condition)
RF   radio frequency
SAR   specific absorption rate

1 Introduction

Radio-frequency (RF) dosimetry studies the human exposure to RF electromagnetic fields (EMF) as well as evaluates the amount of energy absorption inside biological tissues. RF dosimetry is a vital part of the safety assessment of the RF EMF exposure, and it has been studied actively over many decades. In the last ten years, powerful modern computers have allowed increasingly accurate RF dosimetry using computational methods. In this thesis, the performance and uncertainty factors of the numerical algorithms used for RF dosimetry are studied.

1.1 Background

RF dosimetry measures the exposure to RF EMF in terms of the *specific absorption rate* (SAR), which is defined as the absorbed electromagnetic power-loss density divided by the mass density of the tissue. The SAR is closely related to the temperature rise due to the EM power absorption inside the human body, but not directly, as the temperature rise also depends on the thermal parameters and thermoregulation. Recent developments in realistic human body models and thermal models have also made possible direct computational dosimetry of the temperature increase.

The dominant scientifically established adverse health effects of RF electromagnetic fields are thermally related (ICNIRP 1998a, IEEE 2005, ICNIRP 2009), i.e., they are due to excessive absorption of energy which results in elevated temperatures. Several international and national bodies, such as ICNIRP (1998a), have established guidelines and recommendations for the exposure in order to prevent the possibility of short-term thermal damage. The guidelines consist of the *basic restriction limits* which are defined in terms of the averaged SAR. The first of these basic restriction limits has been set for the whole-body averaged SAR to prevent the whole-body heat stress, ensuring that the body-core temperature rise for occupational exposure would be less than 1 °C, with a safety factor of 10. In addition to the whole-body averaged SAR, a separate basic restriction limit has been set for the localized 10 g spatially-averaged SAR to avoid thermal damage in sensitive organs, such as the eyes or the testes.

Direct measurements *in vivo* of the SAR or temperature distributions inside the human body are not possible. Consequently, in addition to the basic restriction limits on the SAR, more easily measurable *reference levels* (ICNIRP 1998a), or maximum permissible exposure levels (IEEE 2005), for the electric and magnetic fields and EM power density outside the body have been defined. Compliance with the reference levels is supposed to ensure that the SAR values inside the body do not exceed the basic restriction limits. Computational dosimetry has been recently used for studying the conservativeness of the reference levels in various exposure scenarios, which has produced

more information for potential improvements and revisions in the reference levels.

Calculations of the human exposure to RF fields require the use of numerical methods. Recently, the *finite-difference time-domain method* (FDTD) (Taflove and Hagness 2005) has been established as the method of choice for computational RF dosimetry (Hand 2008, ICNIRP 2009). The FDTD method provides an approximate time-domain solution for the full Maxwell's equations by using the Yee algorithm (Yee 1966). The FDTD method is a fully explicit difference method with no need to solve matrix equations, which is the main advantage of the FDTD method compared to other numerical methods. There might be more elegant or accurate numerical methods than the FDTD, but in RF dosimetry the FDTD provides good enough results and relatively simple modelling of different kinds of field sources with the smallest computational burden.

A realistic numerical representation of the human anatomy is needed for accurate FDTD simulations of the human RF exposure. During the last few decades, the advances in tomographic techniques, such as the magnetic resonance imaging (MRI) and the computed tomography (CT), have allowed the development of lifelike three-dimensional *human body models*. The numerical human body models used in the RF dosimetry are often referred to as *phantoms*. By the FDTD method, the human body models can be simulated just like any other objects that consist of a heterogeneous mix of lossy dielectric materials: The human body models are divided into a grid consisting of tiny voxels (cells)—for instance, $2 \times 2 \times 2$ mm^3 cubes—after which the tissue type of each voxel is determined, and the electromagnetic material properties of the human tissues, originally determined from animal measurements, are assigned to the voxels. Currently, over a dozen different whole-body models, depicting different individual anatomies including children, have been developed by various research groups around the world.

Computational dosimetry is an important tool for providing background information for the development of exposure standards and guidelines, enabling relatively straightforward calculation of SAR values for all kinds of exposure scenarios. Additionally, dosimetry for the temperature rise may be used to assess the conservativeness of the basic restriction limits. Computational standards for RF dosimetry have been under development recently (e.g. IEEE draft standard 1528.1). The goal of the standardization has been to enable repeatable and robust computational exposure assessment by defining standard numerical algorithms for computational RF dosimetry, in a similar way to standardized measurement procedures.

Computational dosimetry by the FDTD method has a diverse field of applications that require simulating the RF electromagnetic fields inside living beings. The most natural application is the testing of the compliance with the basic restriction limits in various exposure scenarios, ranging from the computational standards-compliance testing of consumer wireless devices to

18

the assessment of exposure during clinical MRI procedures. The computational methods and anatomically realistic models of RF dosimetry may also be applied in the development of wireless devices, whose interaction with the human body can have a great impact on the antenna performance, for example. Health monitoring by implanted wireless devices on the skin or inside the body is another emerging application which requires the know-how from the field of computational dosimetry. In the field of bioelectromagnetics, laboratory studies, which investigate the biological effects of RF fields, require the exposure information provided by computational dosimetry. The computational methods used for RF and thermal dosimetry also have some clinical applications, for example in the planning of hyperthermal therapy for cancer treatment.

1.2   Objectives of the thesis

This thesis concentrates on studying the performance and uncertainty of the numerical methods and models that are used for computational RF and thermal dosimetry. The thesis aims to find what are the best ways to do the FDTD calculations in RF dosimetry. For this purpose, several modelling choices and their effects on the error in simulated results are discussed.

The results of the thesis help to evaluate and identify the possible uncertainty factors and sources of error in computational RF dosimetry, which will produce information for the development of standardized and repeatable computational procedures. Also, the assessment of the uncertainty and accuracy of the methods allows, for example, lessening the computational requirements and improving the accuracy of the simulations.

1.3   Contents of the thesis

The overview of this thesis consists of two parts. Section 2 includes a literature survey of several uncertainty factors and choices of modelling techniques that affect the accuracy of RF dosimetry. Thermal dosimetry is discussed in Section 3, which contains an overview of thermal modelling of the human body under exposure to RF EMF and related uncertainty factors.

A summary of the papers included in the thesis is presented in Section 4. The papers investigate, for example, the computational error in RF dosimetry due to the voxel size (papers IV,V) and the absorbing boundary condition (paper I). Also, it is investigated how the computational error is affected by the choice between the E- and H-cells (papers II,III) or by the choice of the power-loss calculation algorithm (papers III,V). Lastly, the variation of the SAR values with the body model and exposure scenario are studied in paper (VI). Paper (VII) is about low-frequency EM dosimetry, and it is the only paper in which the FDTD method is not used.

2 Error, uncertainty and variation in FDTD SAR calculations

The chain from the real-world exposure case to the final calculated SAR values contains many modelling and approximation phases which may introduce error and uncertainty. In this work, the uncertainty factors are loosely grouped into three types: computational error, modelling uncertainty and real-world variation.

There always exists a unique solution for the Maxwell equations in each physical case, and the *computational error* is the deviation of the numerical solution from that accurate solution. In turn, the *modelling uncertainty* describes how realistically the used models represent the real physical case, i.e., the uncertainty of the simulated case with respect to the actual real-world exposure scenario. Lastly, the *real-world variation* describes how much the results are expected to vary when the actual exposure scenario is altered. A short summary of the main factors affecting these three types of uncertainty is shown in Table 1.

2.1 Computational error

The computational error, which is the part of the uncertainty that is caused only by the numerical method, consists of several factors. In addition to the factors listed below, purely numerical errors such as floating-point error may have some, presumably very slight, influence on the results.

The computational error can usually be reduced by using more computer resources, which includes increasing the resolution, using thicker absorbing boundary conditions, or continuing the simulations longer. The point is to find a good balance so that the computational error is clearly smaller than the estimated modelling uncertainty. The amount of the computational error can be estimated by comparison with an analytical solution (if available) or with a highly-accurate approximate solution by some other numerical method.

2.1.1 Discretization error

The main source of the computational error in the FDTD is the discretization error, which depends on the ratio between the cell size and the wavelength. Reducing the cell size improves the accuracy, but also increases the computational requirements significantly. The general rule of thumb for FDTD simulations is that the maximum cell size should be smaller than one tenth of the wavelength ('$\lambda/10$ rule'). The amount of the discretization error in RF dosimetric calculations may be investigated by performing the same SAR calculations with multiple grid resolutions. If the resulting SAR values differ, it can be concluded that the discretization error is significant.

Table 1: Some uncertainty factors of computed SAR values. Type of uncertainty: 'C' = Computational error, 'M' = Modelling uncertainty, 'V' = Variation in real world

Factor	Type	Notes
Discretization error	C	Depends on the ratio of cell size and wavelength. Sufficiently fine resolution should be used.
Staircasing error	C/M	Is related to the cell size and anatomical accuracy.
ABC reflection error	C	ABCs should be tested and tuned accordingly.
Truncation error	C	Long enough simulation time is necessary.
SAR algorithm	C	Different SAR calculation algorithms may produce varying results.
Anatomical accuracy	M	Is affected by the accuracy of the original anatomical data. Too large voxel size may complicate modelling of thin structures, such as the skin.
Voxelling accuracy	M	Rescaling and rotation of voxel data may cause numerical artifacts.
Material properties	M/V	Material properties of tissues may be uncertain and there may be individual variation.
Antenna modelling	M	Numerical model of the antenna may have large effect on localized (e.g. handset) or whole-body (base station) SAR values.
SAR spatial averaging	M	Various spatial-averaging methods for the SAR have been used.
Body morphology	V	Height affects the whole-body resonance frequency, and weight affects the whole-body averaged SAR.
Local morphology	V	Affects localized SAR values for both the near and far-field exposure.
Posture and grounding	V	May change the whole-body resonance frequency, lesser impact at higher frequencies.

Table 2 is a summary of the recent studies which have, among other things, investigated the effects of the cell size in dosimetric simulations. All of the studies listed in Table 2 have involved the plane-wave exposure of a human body model in the GHz range. Dimbylow and Bolch (2007) studied the whole-body SAR in various child models up to 6 GHz. Their results suggested *inter alia* that 1 mm resolution should be used instead of 2 mm for frequencies higher than ~1 GHz. The SAR values tended to become smaller when a lower resolution was employed. The effect of the resolution on the whole-body SAR and peak spatial averaged SAR in the Visible Human model were discussed in Kühn *et al* (2009) for 835 MHz and 2140 MHz. In that study, the difference between the 1 mm and 2 mm resolutions in the whole-body and spatial-peak SAR values was reported to be minor. Gosselin *et al* (2009) evaluated the impact of the grid resolution on the whole-body and 10 g averaged SAR for the base-station antenna and plane-wave exposure in the frequency range from 450 MHz to 2140 MHz. A cell size of 2 mm was found to be sufficient for all of the frequencies. However, in some special cases the difference between the 2 mm and 1 mm resolutions in the local peak 10 g SAR values could be as large as 20 %. The plane-wave exposure of a newborn model was calculated by Dimbylow *et al* (2010). The effects of the cell size and the choice of the SAR calculation algorithm were investigated for frequencies up to 6 GHz. The calculations suggested that the practical limiting frequencies for the 2 mm and 1 mm cell sizes were about 1 GHz and 6 GHz, respectively. The accuracy of the whole-body SAR was tied in not only with the resolution but also with the algorithm used to calculate the SAR in each voxel. Bakker *et al* (2010) studied the discretization error in a 5-year-old whole-body model using multiple plane-wave exposure scenarios, cell sizes and frequencies up to 5.6 GHz. According to their results, using the 2 mm resolution for frequencies lower than 2 GHz and the 1 mm resolution for higher frequencies resulted in less than 5 % error in the whole-body averaged SAR and less than 12 % error in the peak 10 g SAR. In paper (IV), the effect of discretization error on the peak localized SAR values in the eyes and brain was studied. The results of multiple exposure cases showed that the maximum frequencies for different resolutions were about 2.5 GHz for the 2 mm and 5 GHz for the 1 mm resolution. These frequencies matched closely the $\lambda/10$ rule for the skin tissue, and led to less than a ± 10 % discretization error in the 10 g SAR.

Based on the presented studies, it seems to be relatively safe to use the 2 mm resolution for up to about 2 GHz and the 1 mm resolution for up to about 5 GHz. Of course, it would always be preferable to test the adequacy of the used cell size by calculations if possible. There are a few factors which may affect the discretization error in the SAR values. Firstly, the tissue composition of the body model and the material parameters affect the wavelength inside the body, thus directly changing the ratio of the wavelength to the cell size. For instance, the newborn tissues in Dimbylow *et al* (2010) have higher dielectric values, so the discretization error seems to be larger compared to

Table 2: Differences from fine-resolution result for 2 mm and 1 mm cell sizes at various frequencies. The error values are rounded to 5 % or 10 %. WB = whole-body averaged SAR, 10 g = 10 g averaged SAR.

Reference	SAR value	resolution [mm]	frequency [MHz]	diff. [%]
Dimbylow and Bolch (2007)	WB	2	1000	small
	WB	2	2000	10
	WB	1	6000	10
Kühn *et al* (2009)	WB	2	2140	small
	10 g	2	2140	5
Gosselin *et al* (2009)	WB	2	2140	small
	10 g	2	2140	10
Dimbylow *et al* (2010)	WB	2	1000	5
	WB	2	2000	10
	WB	1	6000	5
Bakker *et al* (2010)	WB	2	1800	5
	WB	1	5600	5
	10 g	2	1800	10
	10 g	1	5600	10
paper (IV)	10 g	2	3000	10
	10 g	1	5000	10
paper (VI)	analytical	2	2100	5*
	analytical	1	4700	5*

*not directly comparable with the other references

the earlier results (Dimbylow and Bolch 2007). Depending on the body model, there may also be special geometrical features—in the fingers and toes, for example—near which the SAR values may be very sensitive to the cell size. Secondly, the error in the SAR values is affected by the choice of the SAR calculation algorithm (paper VI). Finally, the choice between the E- and H-cell approaches may affect the amount of discretization error (papers II and III).

2.1.2 Staircasing error

The basic FDTD is limited to rectangular cells, which induces the staircase approximation error. This error is a kind of modelling uncertainty, caused by the limitations of the computational method. The staircase approximation error is important when simulating metal structures (Holland 1993, Taflove and Hagness 2005), but the significance of the error is not yet fully known for heterogeneous body models. The available anatomically realistic models have traditionally consisted of rectangular voxels, so taking curved bound-

Reality   FDTD simulation

$\Rightarrow$

ABC
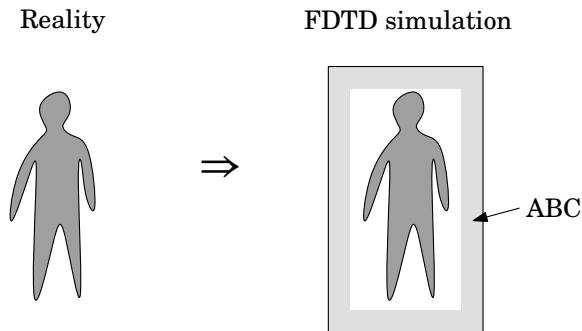
Figure 1: In the FDTD method, free space is modelled by surrounding the simulated object with a layer of absorbing material.

aries into account in the computational method has been unnecessary. Lately, anatomically realistic surface-based models have been developed (Christ *et al* 2010b), which might make studying the staircase error more relevant. The amount of the staircase approximation error was estimated in the author's Master's thesis (Laakso 2007) by calculating the SAR values in small homogeneous muscle spheres. The results suggested *inter alia* that in spheres with radius larger than 14 cells, the error in the whole-sphere averaged SAR was less than 1 %. In paper (IV), the comparison between different resolutions showed that for sufficiently small frequency, the 1 mm resolution gave a very close match with the 0.5 mm resolution results, which suggests that the staircase approximation error was small. However, for the 2 mm resolution the error might be more significant. In addition to causing staircasing error, the rectangular FDTD grid also complicates the modelling of the field sources, such as the plane waves incident from oblique angles, or antennas that are not aligned with the computational grid.

2.1.3 Absorbing boundary conditions

In the FDTD method, modelling the free space must be done by terminating the calculation domain by absorbing boundary conditions (ABCs, Figure 1). One significant source of error may be due to the reflections from the absorbing boundaries, affected by the choice of the ABC and its parameters. Today, the most commonly used absorbing boundaries are the perfectly-matched-layer (PML) type ABCs, including the split-field PML (Bérenger 1994), the uniaxial PML (UPML, Sacks *et al* 1995, Gedney 1996), and the convolutional PML (CPML, Roden and Gedney 2000). The performance of these three common boundary conditions in FDTD-SAR calculations has been studied, for example, in (Findlay and Dimbylow 2006a), in (Wang *et al* 2006a, Kühn *et al* 2009) and in paper (I), respectively. Lazzi *et al* (2000) studied the localized exposure of the head and showed that the size of the calculation domain could be truncated to a small fraction of the whole head by using PML boundaries,

with a very small error in the SAR values near the exposure source. In Wang *et al* (2006a), the reflection error of the ABCs in SAR values was found to be significant. However, the findings in paper (I), Lazzi *et al* (2000) and Findlay and Dimbylow (2006a) are sufficient to show that it is possible to create ABCs which perform very efficiently, making the error in the SAR values negligibly small.

The performance of the ABCs should be tested by using a similar procedure to Findlay and Dimbylow (2006a). In that procedure, the whole-body averaged SAR was calculated while varying both the ABC-object distance and the thickness of the ABC. Small variation in the SAR for sufficiently thick ABCs implicated that the ABCs performed well. The procedure in paper (I), which involved only the distance variation, is not always (at very low frequencies compared to the cell size) enough to guarantee good performance (unpublished observations 2010). The performance of the ABCs depends also on the size of the object and the frequency. For example, the split-field PML in Findlay and Dimbylow (2006a) was tested only for a whole-body human model, and it seems likely that the same ABC might not perform as well for small objects (paper V). On the other hand, the CFS-PML in paper (V) was not tested for the combination of a whole-body model at low (< 100 MHz) frequency, in which case the CFS-PML actually fails with the presented parameters (see the Errata for a solution).

2.1.4 Postprocessing and interpretation of the results

A kind of computational error, the truncation error, may be caused by incorrectly stopping the FDTD simulation too early, when the steady-state has not yet been reached (sinusoidal excitation), or when the fields have not yet attenuated enough (pulse excitation). Actually, this behaviour of the fields also exists in the real world. The truncation error only becomes evident when the results are postprocessed, for instance, when the complex field values are computed from the time-dependent values. In Kühn *et al* (2009), uncertainty in SAR values due to this error was approximated to be 0.2 dB. For the usual exposure calculations, the truncation error can be reduced by increasing the amplitude of the source signals gradually over a few periods in the beginning of the simulations, or by just continuing the simulations longer. The truncation error might become more important if too fine resolution with respect to the frequency were used, or if there were strongly resonating structures, both of which conditions may result in extremely long simulation times.

Postprocessing, i.e., how the results are interpreted, may also bring additional computational error. This includes the method by which the power-loss density is calculated from the FDTD electric field (paper VI). Dimbylow *et al* (2008) compared the whole-body averaged SAR calculated by three different institutions using four body models. The differences between the calculations were generally within 5 % at lower than 1 GHz frequencies. The divergence of

the results increased at higher frequencies, and the differences in the whole-body averaged SAR at 3 GHz could be as large as 10–30 %, depending on the model. The SAR calculation algorithm and the dielectric properties of the skin and fat tissues were pointed out to be the most important factors influencing the whole-body SAR. Changing the SAR calculation algorithm could cause up to a 15 % difference in the whole-body averaged SAR at high frequencies. Similar behaviour was also observed in paper (III) and in Dimbylow *et al* (2010). In paper (VI), the divergence of the SAR values due to the different SAR calculation algorithms was studied further. It seemed that both the magnitude and direction of the discretization error in the SAR values is affected by the choice of the SAR algorithm. For example, one of the three studied SAR calculation algorithms, the trapezium algorithm, always produced the highest SAR values and had the tendency for overestimation. On the contrary, another algorithm, the mid-ordinate algorithm, often underestimated the SAR values.

2.2 Modelling uncertainty

The modelling uncertainty describes how the used computational models deviate from the real physical scenario. Modelling uncertainty is introduced when the physical parameters or models are inaccurate or there is uncertainty in the measured input values. The modelling uncertainty also includes the variations in results caused by different choices, simplifications and approximations made by the judgement of the user, or by the solver software.

Unlike the computational error, the modelling uncertainty cannot usually be lessened easily, and even estimating its range may be difficult. Sometimes, the range of the modelling uncertainty can be estimated by variation analysis, by testing how sensitive the results are to small changes in the model parameters. In some cases such as the liquid phantoms, rough verification by measurements is possible (Joseph and Martens 2005, Ilvonen *et al* 2008, Gosselin *et al* 2009).

2.2.1 Anatomical body models

Sufficiently representative models of the electrical properties of the human anatomy are needed for RF dosimetry. During the last few decades, the advances in tomographic techniques, namely the magnetic resonance (MR) imaging and the computed tomography (CT), have allowed the development of anatomically lifelike human body models. Several whole-body models have been developed for both non-ionizing and ionizing radiation dosimetry and radiology (Zaidi and Tsui 2009). The whole-body models used in RF dosimetry in recent years include (Hand 2008), for example, the male voxel model (Mason *et al* 2000) constructed using the CT, MR and cryosection images of a male cadaver from the US National Library of Medicine's Visible Human Project
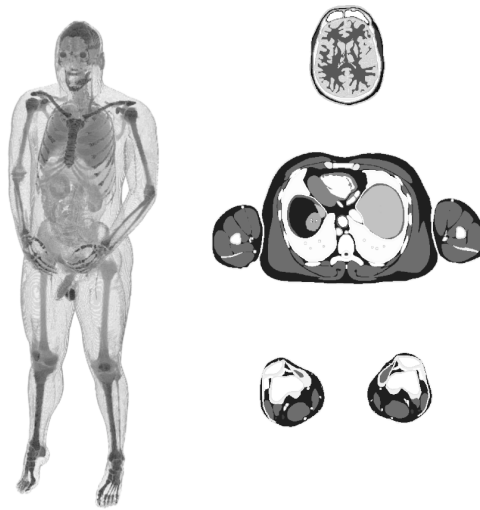
Figure 2: The anatomically realistic voxel model based on the Visible Human Project. Three transverse cross-sections of the model are shown on the right.

(Spitzer and Whitlock 1998, Ackerman 1998) (Figure 2); the Zubal head and torso model based on CT and MR images (Zubal *et al* 1994); voxel models constructed from MR images, such as Norman (Dimbylow 1997), Naomi (Dimbylow 2005b), Taro and Hanako (Nagaoka *et al* 2004); the Korean male voxel model constructed from colour photographic images of cryosection slices (Kim *et al* 2008); and the surface-based Virtual Family models of two adults and two children constructed from MR images (Christ *et al* 2010b).

The tomographic techniques produce accurate description of the anatomy of a specific human subject. However, the resulting voxel models are rigid and difficult to modify. In addition, the imaging of the subjects is done in the supine position, which causes a shift of the internal organs compared to the upright position. Cassola *et al* (2010) designed female and male adult whole-body phantoms without tomographic images by using the tools originating from the fields of computer graphics and animated films, and freely available 3D models of individual organs. This demonstrates the possibilities for creating body models of different height, weight and posture. Posture transformation technique for voxel models has been proposed (Nagaoka and Watanabe 2008). The technique utilizes methods originating from the computer-aided design (CAD) and computer graphics, and allows changing the posture of the voxel model while maintaining the continuity of tissues. An improved model by the same authors (Nagaoka and Watanabe 2009) solves some technical disadvantages of the previous technique, resulting in a relatively straightforward process that is, in theory, applicable to any voxel model. Potentially, a similar kind of procedure could possibly be used for morphing voxel models to different body shapes, heights and weights.
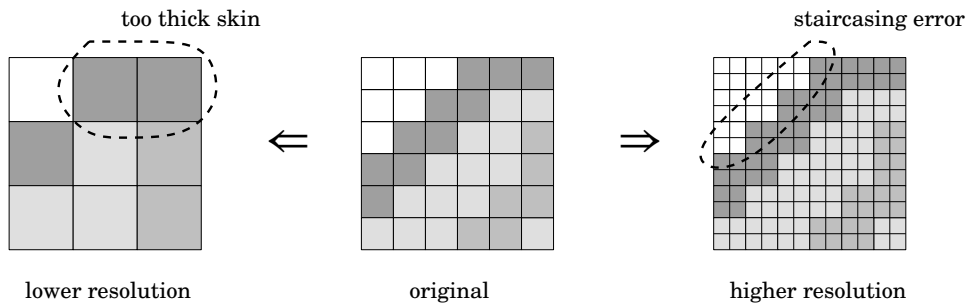
Figure 3: Increasing or decreasing the resolution of voxel models causes various numerical artifacts.

Constructing the three-dimensional anatomical models from images that are two-dimensional is a difficult and time-consuming process. Various algorithms have been developed to facilitate the process, but the manual segmentation of tissues is still laborious and time-consuming (Zaidi and Tsui 2009). Resolution of the two-dimensional image slices and the distance between the slices determines the maximum level of the anatomical detail in the model, so the actual anatomical resolution might not be the same as the resolution of the resulting three-dimensional voxel model. It is important that the resolution is sufficient for representing all relevant anatomical details. Limited resolution is problematic for modelling thin layer tissues such as the skin, the volume of which is overestimated in many voxel models (Zaidi and Tsui 2009). The layer structure of the skin may influence the peak localized SAR values greatly (Drossos *et al* 2000, Christ *et al* 2006).

2.2.2 Altering the voxel grid

For high frequencies, the required cell resolution for the FDTD might be higher than the resolution of the anatomical model. This requires rescaling of the voxel data to a higher resolution, which may cause additional staircase approximation of curved boundaries, illustrated in Figure 3. The error caused by this rescaling was investigated, for example, by McIntosh and Anderson (2010) who modelled a sphere with a 0.5 mm cell size and another sphere with 2 mm cells which were then re-meshed to 0.5 mm cells. Under the exposure to a 10 GHz plane wave, the difference between the two spheres was around 5–8 % for both the whole-body and peak 10 g SAR. Hirata *et al* (2007c) reported using interpolation techniques for reducing the staircasing effect when increasing the model resolution, although no details are given.

When the studied wavelength is long compared to the voxel size in the anatomical model, it may be advantageous to scale the voxel data down to a lower resolution, which may be done by various different ways (Van de Kamer *et al* 2001). Figure 3 shows an example of reducing the resolution by the 'winner-takes-all' method, which results in a loss of detail and overestimation

of the thickness of thin-layer structures.

Different voxelling problems may arise when studying the near-field exposure due to antennas in an arbitrary position with respect to the body model. In such a case, it is usually advantageous to align the antenna structures to the FDTD grid and rotate the body model to prevent the staircase error when modelling the antenna. Rotating the body model requires re-meshing the voxel data into a new rotated grid which may cause various numerical artifacts in the new voxel models (Beard and Kainz 2004).

2.2.3 Dielectric properties

The dielectric properties of tissues used in the computational dosimetry are usually based on the widely-used four Cole–Cole dispersion model (Gabriel *et al* 1996c). The model has been derived by fitting the four Cole–Cole dispersion parameters to the measured values of animal tissue (ovine and porcine), human autopsy materials, and human skin and tongue *in vivo* (Gabriel *et al* 1996b); and the values found by a literature review (Gabriel *et al* 1996a). There may be a significant individual variation in the dielectric properties— the variation in tissue properties within a species may even exceed variations between different species (Gabriel *et al* 1996b). The biological tissues are inhomogeneous, and natural variation in the structure or composition inside a single tissue causes about ± 5–10 % variability in the dielectric properties above 100 MHz (Gabriel *et al* 1996b). This random variability constitutes the main source of uncertainty for the tissue data, exceeding the contributions from the measurement procedure and instrumentation (Gabriel and Peyman 2006).

Keshvari *et al* (2006) studied how sensitive the SAR values in the head are to increasing the permittivity and conductivity values by up to 20 % in the frequency range from 900 MHz to 2450 MHz. The results showed that the SAR values in the ear and eye region could both increase or decrease, with the maximum variation smaller than 20 % and the usual variation only about 5 %. It was suggested that the sensitivity of the SAR values depends on the individual anatomical details of the models. Dimbylow *et al* (2008) showed that changing the dielectric properties of the skin and fat tissues from wet skin and non-infiltrated fat to dry skin and infiltrated fat, respectively, could have a significant effect on the whole-body averaged SAR in an adult male model. Above 1 GHz this could increase the whole-body averaged SAR by up to 15 %. However, the choice of these material parameters only had a minor effect at lower frequencies.

The most important aspect affecting the dielectric properties is the water content of tissues (Gabriel *et al* 1996c). The tissues in young children have higher water content than in adults, so the permittivity and conductivity values of tissues may be higher in children. The decrease of the permittivity and conductivity of various tissues with age was demonstrated in rats aged
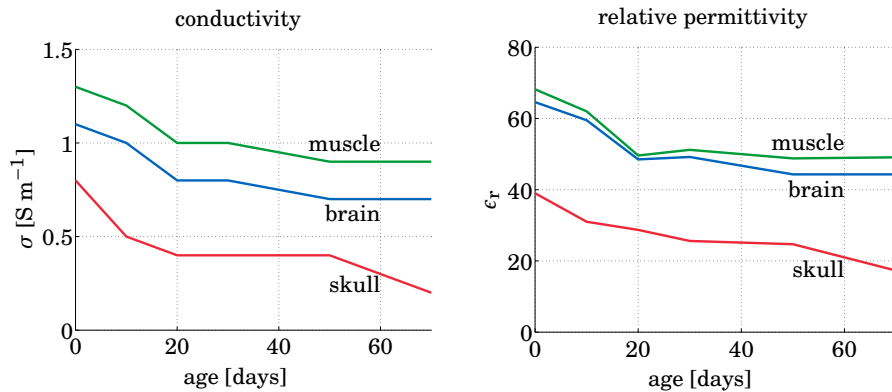
Figure 4: Age-dependence of the conductivity and permittivity of some rat tissues at 900 MHz (Peyman *et al* 2001).

from 0 to 70 days (Peyman *et al* 2001), see Figure 4. The data was further validated and extended to lower frequencies by Gabriel (2005). Peyman *et al* (2009) measured the dielectric properties in several ageing porcine tissues which are regarded as good substitutes for the human tissues. The results showed a significant reduction in the permittivity and conductivity values in 10 out of the 15 measured tissues.

Even though there may be significant decreases in the dielectric properties with age, the variation in SAR values with age may still be small. Using the adult tissue properties instead of 3-year (or older) child tissue data seems to cause only a minor and non-systematic error in the localized SAR values in the head (Keshvari *et al* 2006, Wang *et al* 2006b, Peyman *et al* 2009, Christ *et al* 2010a). Wang *et al* (2006b) derived an approximate formula for the age-dependence of the dielectric properties and calculated the SAR due to a mobile-phone model at 900 MHz using 3- and 7-year old child head models. It was found out that the age-dependence of the dielectric parameters is unlikely to have a significant impact on the SAR results. Peyman *et al* (2009) performed simulations of two child head models exposed to a mobile phone model. Using the adult tissue properties instead of the child tissue data (about 1–4 or 11–13 years old) had only a minor impact on the SAR values in the head. In Christ *et al* (2010a), the mobile-phone exposure in multiple head models was studied, and no systematic changes in the peak 10 g SAR due to the age-dependent dielectric properties (Peyman *et al* 2009) were found. For the whole-body exposure of the newborn, the impact of the higher water content may be more significant. Dimbylow *et al* (2010) calculated the SAR in a newborn model based upon a surface representation of the organs of the body. The permittivity and conductivity values of the model were the adult values multiplied by factors derived from the Peyman *et al* (2001) data for rats. Using the newborn tissue parameters resulted in +15 % higher whole-body SAR at the resonance frequency compared to using the

adult parameters.

2.2.4 Exposure sources

Plane waves are one of the most easy to implement field sources in FDTD, and have only a few easily characterised variables, such as the direction and polarization. On the contrary, the exposure to hand-held devices features a myriad of different variables. The SAR results may be very sensitive to small changes in modelling the antennas and their positioning with respect to the body model. For example, the errors and differences in judgement during the positioning of the source mobile phone were suggested to be the reason for the result that the maximum 10 g SAR values in the same head model simulated by 14 different institutions in the same exposure scenario had up to 30 % standard deviation (Beard *et al* 2006). This variance is comparable to that from the measurements in liquid phantoms. Also, the variance is as large as the standard deviation of the 10 g SAR in various head models induced by the same near-field source (Wiart *et al* 2008). Positioning and modelling the hand holding the mobile phone may be an another significant source of variation.

For the modelling of fine metallic structures, a very fine cell size or special techniques for the modelling of thin structures are needed. Metal structures are more sensitive to the staircase effects compared to the lossy dielectric body models. A number of different methods for reducing the staircase approximation error, such as the contour-path techniques are available (Taflove and Hagness 2005). However, implementing these techniques by hand for real-like devices would be an extremely tedious process, and researchers using their own FDTD codes often have to make do with simplified source models. On the other hand, commercial FDTD software have automatic methods for importing and simulating CAD models of realistic devices, far beyond the capabilities of most research or university FDTD codes. However, because getting the CAD models of real devices from the manufacturers may be problematic, and given the large uncertainties related to the antenna modelling and positioning, the simplified models may still be sufficiently representative for the generic exposure assessment.

2.2.5 Spatial averaging of SAR

When comparing the results between different studies it is important that the SAR values would be averaged exactly the same way in all studies. However, the lack of exact description of the spatial SAR averaging method in ICNIRP guidelines (ICNIRP 1998a,b) leaves some room for interpretation. The basic restriction limit for the 10 g SAR has been set up to provide protection against excessive temperature rise in sensitive body parts, such as in the eyes. Hence, in theory the SAR averaging algorithm should be defined such that the averaged SAR is in a good correlation with the temperature

distribution inside the body.

Recently, using cubically-shaped averaging volumes (IEEE 2005, 2002) has become the standard way for averaging the SAR. However, from a purely physical perspective, the use of cubical averaging volumes is somewhat questionable. Since, for example, spherical volumes would clearly provide a more realistic match with the resulting temperature rise. Moreover, the IEEE (2005) standard actually requires that the averaging cubes should align with the coordinate axes of the computational procedure, making the averaged SAR dependent on the choice of the voxelling of the body models. By the IEEE (2002) specification, the SAR averaging cubes need to be treated specially near the surface of the body, which leads to a poor correlation between the SAR and temperature elevation (McIntosh and Anderson 2010). High frequencies over 6 GHz are particularly problematic for cubical averaging (IEEE (2005) use spatially-averaged SAR only up to 3 GHz), because of the short penetration depth of the microwaves and the highly superficial SAR values (McIntosh and Anderson 2010).

Several studies include comparison of various SAR averaging methods for microwave exposure of the head (Hirata *et al* 2006a, Wainwright 2007, Flyckt *et al* 2007). It is clear from the results that the choice of the spatial-averaging scheme has a great impact on the resulting SAR values, so care is needed when comparing results from different studies. Hirata and Fujiwara (2009) investigated the correlation between the cubically-averaged SAR with a varying cube size and the temperature rise in the head under exposure to a dipole antenna in the range from 1 GHz to 6 GHz. The SAR averaged over the 10 g cubes was reasonably well correlated with the temperature rise in the whole frequency range. In paper (IV), it was shown that the peak cubically-averaged 10 g SAR in the eye correlates well with the peak temperature rise in the lens. The correlation between the temperature rise, peak spatially-averaged SAR and incident power density was investigated using one-dimensional layered models (Anderson *et al* 2010) and anatomically realistic adult and child models (McIntosh and Anderson 2010) in the frequency range 1–10 GHz. It was not clear from the results which of the incident power density or the 10 g SAR was correlated better or worse with the temperature increase between 3 and 10 GHz.

In all the papers in this thesis, the spatial averaging of the SAR has been done by using the procedure specified in IEEE (2002). The procedure describes how to define the SAR averaging cubes for each FDTD cell, including the special averaging procedure for the cells that are located on the air-body boundary. In this thesis, the sizes of the averaging cubes have been further fine-tuned such that their mass is exactly 10 g (Caputa *et al* 1999). The above procedure is computationally demanding—in fact, during the preparation of paper (IV), calculating the 10 g averaged SAR took more time than calculating the steady-state temperature increase at high resolutions.

2.3 Real-world variation

In this work, the real-world variation means the changes in results due to the different physical conditions, such as the individual variation in morphology, and also the variation in the electromagnetic exposure scenario. Unlike the computational error and modelling uncertainty, the real-world variation is not error, as it exists also in the real world. The variation is important when developing standards and guidelines for limiting the exposure, because the limits should be valid for all kinds of individuals in all common exposure scenarios.

2.3.1 Variations in body morphology

The whole-body exposure studies that have included multiple human models have allowed the assessment of the effect of the model morphology on the whole-body SAR values. The results for the whole-body exposure for frequencies up to 3 GHz are quite consistent between various studies (Conil *et al* 2008, Dimbylow *et al* 2008, Kühn *et al* 2009, Bakker *et al* 2010)(paper V) . Typically, the models with a larger weight have a smaller whole-body averaged SAR. For the models with a small weight, such as children, the reference levels may violate the basic restriction limits in the 1 to 3 GHz range. For the vertically-polarized plane-wave exposure at a constant incident power density, the largest whole-body averaged SAR values happen near the whole-body resonance frequency, which occurs at typically below 100 MHz frequencies for adults, depending on the height of the model. Although the results between various studies are consistent, some differences exist. It is not fully clear which part of the variation is due to the real-world individual morphologies and which is due to the modelling differences or computational error. The real-world individual variation in the dielectric material properties might also affect the SAR, which was discussed in Section 2.2.3.

Some studies have investigated which morphological factors affect the whole-body averaged SAR. Hirata *et al* (2007b) studied the whole-body SAR in the heterogeneous and homogeneous Norman model and cuboid phantoms, and corresponding scaled child phantoms. The results suggested that in the GHz region (above 1 GHz), for models of the same mass, the surface area of the model is the dominant factor affecting the whole-body SAR. However, the same was not true in the whole-body resonance region. Kühn *et al* (2009) studied the plane-wave exposures of four models with six incident directions. Normalizing the whole-body averaged SAR to the ratio of the 'visible' area divided by the weight was able to partly explain the variation between the individual models in the GHz range. The same is also true for the frontal base-station antenna exposure as was shown by Gosselin *et al* (2009), who studied the exposure of three adult models from 450 MHz to 2140 MHz. Habachi *et al* (2010) studied the whole-body averaged SAR in 12 anatomical voxel models,
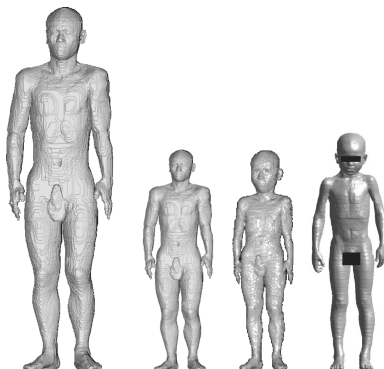
Figure 5: An adult model (Nagaoka *et al* 2004), a uniformly-scaled 5-year-old child model, a morphologically-scaled 5-year-old child model (Nagaoka *et al* 2008), and a realistic 6-year-old child model (Christ *et al* 2010b).

and 18 morphologically-scaled 5-, 8- and 12-year old child models. The exposure source was a vertically polarized plane wave incident from the front at 2.1 GHz. The results showed that the accurate estimation of the whole-body SAR requires information about not only external morphology factors (height, weight and body surface area) but also about the internal morphology factors, such as the muscle and fat proportions. Hirata *et al* (2010) derived a simple formula for estimating the whole-body SAR at the whole-body resonance frequency (ratio of the model height to the wavelength is 0.38–0.40). According to the formula, the whole-body SAR at the resonance frequency is inversely proportional to the body mass index, and it also depends on the body fat percentage. Using the formula together with the statistical data of the Japanese population showed that the variability of the whole-body SAR due to the body shape is about 30 % for humans of the same age.

2.3.2 Exposure of children

Until recently, there have been few whole-body models of children available, so SAR calculations of children have been performed using uniformly-scaled adult body models (Dimbylow 2002, 2005a, Findlay and Dimbylow 2006b) or morphologically-scaled adult models (Nagaoka *et al* 2008, Conil *et al* 2008), see Figure 5. Nagaoka *et al* (2008) showed that the whole-body averaged SAR values in morphologically correct and uniformly-scaled child models are not significantly different. However, large differences in the tissue-averaged SAR were reported. Recently, anatomically realistic whole-body models of children have been developed. It seems that the whole-body averaged SAR in anatomically realistic child models is consistent with the whole-body SAR in scaled adult models (Dimbylow and Bolch 2007, Kühn *et al* 2009).

The general public reference levels (ICNIRP 1998a) should be valid for all

kinds of individuals under different exposure scenarios. The reference levels have been derived from the basic restriction limits for adults so they may not be directly applicable to small children. It is well known from several recent studies that the reference levels may violate the basic restriction limits in the GHz range for children, i.e., incoming power density or field strength that is below the reference level may lead to SAR values that exceed the basic restriction limits. Dimbylow *et al* (2010) calculated the SAR in a newborn model, an important limiting case, exposed to plane waves incoming from various directions. The results showed that the reference level violates the basic restriction limits at 250 MHz, the whole body resonance, and in the range from 700 to 2450 MHz. It should be noted, however, that the basic restriction limit for the whole-body averaged SAR might actually be more conservative for children when considering the body-core temperature rise (Hirata *et al* 2008a).

There is uncertainty regarding the risk posed to the foetus by strong RF exposure of pregnant women. Elevated temperatures at the foetus during certain stages of pregnancy may cause developmental effects. Because of this, the plane-wave exposure of pregnant women at different stages of pregnancy have been investigated in several studies, for example, (Nagaoka *et al* 2007, Dimbylow *et al* 2009, Kawai *et al* 2010). Several pregnant woman and foetus models were compared in Dimbylow *et al* (2009), and the results showed that the ICNIRP reference levels are very conservative for the 10 g SAR in the foetus. Also, the foetus-averaged SAR is smaller than the whole-body averaged SAR of the mother. MRI, which features significant exposure to the RF fields, is increasingly being used to image both the mother and foetus. The SAR values in the mother and foetus during MRI procedures has been calculated in various studies (Hand *et al* 2006, 2010, Kikuchi *et al* 2010). The temperature rise in the foetus due to SAR has been simulated with a discrete vasculature thermal model (Hand *et al* 2010) and with a model of the thermoregulatory system (Kikuchi *et al* 2010).

2.3.3 Variations in posture and exposure scenario

Most studies have considered only the exposure to a vertically polarized plane wave incident from the front, the exposure setup that results in the strongest whole-body resonance for models in the standing posture. The horizontally polarized exposure is not able to excite the main whole-body resonance so the whole-body SAR values are significantly smaller compared to the vertically polarized plane waves near the whole-body resonance frequency. The same is true for the waves incoming from the above or below of the model. In the whole-body resonance range, the incoming direction in the transverse plane seems to have only a minor effect on the whole-body averaged SAR. The side exposure may actually produce a slightly higher whole-body averaged SAR than the frontal exposure (Kühn *et al* 2009).
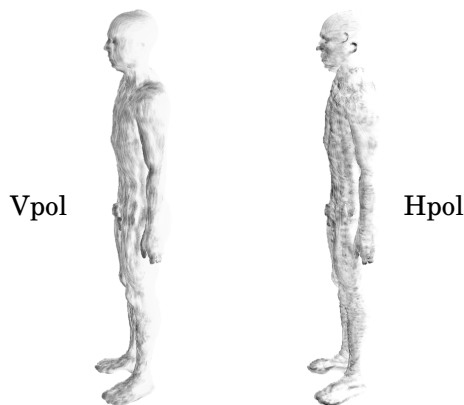
Figure 6: Frontal plane-wave exposure of the Norman model at 3.5 GHz for the vertical (left) and horizontal (right) polarizations (paper V). The darker areas depict higher pointwise SAR values. The sides of the head, arms and legs are more exposed with the horizontal polarization, and the topsides of the head, shoulders and feet are more exposed with the vertical polarization.

In the GHz range, the frontal exposure has the highest whole-body averaged SAR (Kühn *et al* 2009)(paper V), so when looking for the worst-case exposure scenario, it is sufficient to simulate only the frontal exposure case. Above 2 GHz, horizontally polarized plane waves result in a higher whole-body averaged SAR than vertically polarized waves with the same power density (paper V), especially for the irradiation from the side. The difference between the vertical and horizontal polarizations seems to increase with the frequency. Hirata *et al* (2009) performed the SAR calculations for up to 6 GHz frequencies using morphologically scaled infant and child models, with ages ranging from 9 months to 7 years. They suggested that the higher whole-body SAR value with the horizontal polarization is attributed to the component of the body surface area perpendicular to the electric field of the incident wave. However, the results in paper (V) show that the whole-body SAR is more sensitive to the azimuth angle with the vertical polarization, which contradicts the explanation by Hirata *et al* (2009). A better explanation may be derived by the analogy with a conducting surface. Namely, a wave with a perpendicular electric field is able to propagate along a conducting surface, whereas a wave with a parallel electric field is not. So it seems reasonable that the horizontally polarized wave is better able to propagate around the body along the sides, and the vertically polarized wave along the soles and the top of the head. Because the sides of the body have a larger surface area, the horizontal polarization results in a higher whole-body averaged SAR. Figure 6 shows an example of the SAR distributions for the horizontal and vertical polarizations.

Most anatomically realistic voxel models are in the upright standing posture, with the arms by the side of the body. Change in the posture may

cause changes in the whole-body resonance frequency. Several postures were studied in the whole-body resonance frequency range by Findlay and Dimbylow (2005). Nagaoka and Watanabe (2008) developed an advanced posture transformation method and used it to study the whole-body SAR in sitting Japanese models in the frequency range from 10 to 3000 MHz. In paper (V), a homogeneous model in 6 postures was used to study the effects of the posture on the whole-body averaged SAR. Based on the results of the above three studies, it seems that, in the GHz range, the whole-body averaged SAR in the different postures is comparable to that of the original standing models. In the whole-body resonance region, the effect of posture is much more significant, for example, altering the whole-body resonance frequency. In addition to changes in posture, also using grounded conditions may have a large impact on the whole-body averaged SAR values in the whole-body resonance region. Grounding, i.e., adding a conducting ground plane below the model's feet, decreases the whole-body resonance frequency, because the body effectively becomes longer with respect to the wavelength. However at frequencies higher than the whole-body resonance region, the importance of grounding becomes insignificant (see e.g. Dimbylow (2002)).

The whole-body exposure to the near field of base station antennas is a more complex problem than the plane-wave exposure. Base station antennas may vary greatly in sizes and shapes, ranging from the human-sized outdoor antennas to the small indoor picocell antennas, which naturally causes a large variation in the SAR values between different antennas. Smaller antennas tend to produce a more localized SAR distribution, so the peak 10 g averaged SAR is larger relative to the whole-body averaged SAR. Gosselin *et al* (2009) calculated the SAR at frequencies 450–2140 MHz using six large (length 130–190 cm) base station antennas and three body models. The basic restriction limit on the whole-body averaged SAR was in most cases more restrictive than the limit for the localized SAR. On the contrary, in Lacroux *et al* (2008), where the exposure of two male models to a smaller 2140 MHz antenna model (length 56 cm) was simulated, the peak 10 g SAR was in most cases the limiting factor. Smaller indoor picocell antennas rarely have enough output power to even theoretically exceed the whole-body averaged SAR limits. Antennas with a wider horizontal half-power beam width provide a better compliance with the basic restriction limits, because a smaller portion of the radiated power is absorbed in the body (Gosselin *et al* 2009). The antenna near field is highly inhomogeneous, so there may be problems in applying the reference levels (which have been derived for the plane wave exposure) for testing the compliance with the basic restriction limits (Joseph and Martens 2005, Martínez-Búrdalo *et al* 2005, Lacroux *et al* 2008, Ilvonen *et al* 2008). Consequently, simple formulae have been developed for estimating the SAR near base-station antennas (Thors *et al* 2008, 2009).
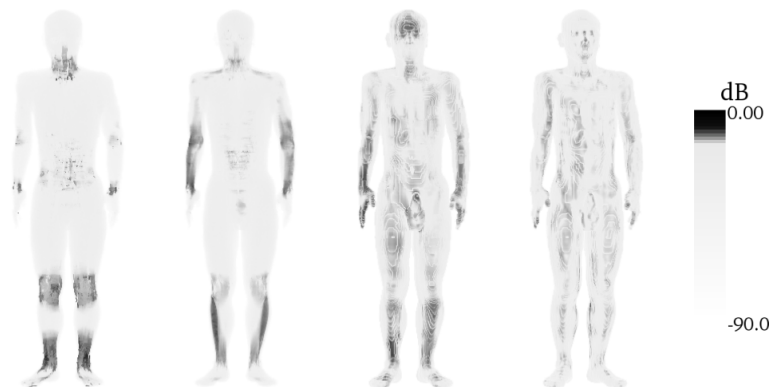
Figure 7: Frontal plane-wave exposure of the Taro model (Laakso and Uusitupa 2010). From left to right: 70 MHz, 300 MHz, 900 MHz and 2450 MHz. The maximum pointwise SAR value corresponds to 0 dB, separately at each frequency.

2.3.4 Variation in localized SAR

While the variation of the whole-body averaged SAR is relatively systematic—depending on, for instance, the frequency, height and posture of the model—the variation of the localized 10 g SAR values does not have such a clear pattern. Large variation in the 10 g SAR results depending on the individual morphology has been reported in several studies that have employed multiple head models exposed to mobile-phone frequency antennas (Christ and Kuster 2005, Kainz *et al* 2005, Keshvari and Lang 2005, Wiart *et al* 2008, Christ *et al* 2010a). Dependence of the localized SAR on morphology is significant not only for the near-field but also for the plane-wave exposure. For example, the SAR results for the plane-wave exposure in Hirata *et al* (2007c) and paper (IV) showed significant differences between two different head models. The conclusion that the 10 g SAR induced by the same source in different head models has a 30 % standard deviation (Wiart *et al* 2008) seems to be a reasonable approximation for the variation. In addition to the variation in morphology, the real-world individual differences in the dielectric material properties might also cause a variation of the localized SAR, which was discussed in Section 2.2.3. As said, the localized SAR values calculated in various head models vary greatly, but there seems to be no systematic difference in the maximum 10 g SAR values between adult and child heads (Christ and Kuster 2005, Keshvari and Lang 2005, Christ *et al* 2010a). However, under the exposure to the mobile phone radiation, the brain tissues and the eyes might be higher exposed in children than in adults (Wiart *et al* 2008, Christ *et al* 2010a), which seems very reasonable because the children have a smaller thickness of the pinna, skin and skull.

The location of the maximum 10 g SAR tends to be deeper in the body at

lower frequencies and more superficial at higher frequencies. In the whole-body resonance region, the largest SAR values are typically located near the ankles, knees or neck (Dimbylow 1997, Nagaoka *et al* 2004, Bakker *et al* 2010). In the GHz region, the maximum is typically located in the fingers, toes, chin, nose, pinnae, penis, or testicles (Kühn *et al* 2009, Bakker *et al* 2010)(paper V), and the location is strongly dependent on the incident direction of the plane wave. For the near-field exposure to base station antennas, the locations of the peak SAR naturally depend on the positioning of the antenna, but often they seem to be in the above-mentioned locations (Lacroux *et al* 2008, Gosselin *et al* 2009). Figure 7 shows examples of the localized SAR distributions at four frequencies for the frontal plane-wave exposure. At 70 MHz, the whole body is resonating, and the highest SAR values are located in the ankles. At 300 MHz, the limbs are highly exposed, apparently due to some partial-body resonances. At higher frequencies the SAR distribution becomes more superficial. At 900 MHz, the SAR is more uniformly distributed compared to the case at 2450 MHz, where there are SAR hot spots in the fingers and nose, for example.

3   Temperature rise due to EM power absorption

Absorption of electromagnetic power inside the human body causes increases in the tissue temperature. The temperature increase may be calculated after the electromagnetic field distribution inside the human body has been solved by the FDTD. The EM power-loss distribution calculated from the electric field acts as the source term for the thermal problem, but otherwise the electromagnetic and thermal problems are usually assumed to be independent of each other. Actually, the dielectric properties of biologic tissues are temperature dependent, and therefore, the power-loss distribution could change as the RF heating proceeds. However, this effect may be neglected for relatively small temperature elevations, as is expected for common RF exposure cases (Lin and Bernardi 2007).

The thermal problem is computationally smaller compared to the electromagnetic problem. There is only one scalar unknown—the temperature T—instead of the six unknown field components in the electromagnetic problem. Also, there is only need to solve the temperature distribution inside the body, so implementing absorbing boundary conditions or external field sources is not needed.

Contrary to the electromagnetic problem, where the human body is passive, in the thermal problem the human thermoregulatory system actively attempts to maintain a thermal homoeostasis. Consequently, the equations for the temperature elevation are generally nonlinear, such that increasing the temperature to higher levels requires a relatively greater EM power than lesser temperature elevations. If the thermoregulatory system is not fully capable of dissipating the heat load, there may be potentially harmful increases in local tissue and body-core temperatures.

This section consists of an overview of the equations and models that may be used to simulate the heating by RF power absorption. The uncertainty factors and required assumptions will be discussed without going too deep into the details. Lastly, an efficient computer implementation of the steady-state bioheat equation is presented.

3.1   Bioheat equation

The bioheat equation was originally proposed by Pennes (1948) for analyzing the temperature distribution in a resting human forearm. The equation is commonly used to model the temperature rise due to the electromagnetic power absorption. In this work, the thermal model by Bernardi *et al* (2003) will be considered. The model has been used in several recent studies on the subject. It combines the bioheat equation and thermoregulatory models, allowing the thermal modelling of the whole human body. A more thorough explanation of the model may be found in Lin and Bernardi (2007).

The bioheat equation is a partial differential equation

$$C(\mathbf{r})\rho(\mathbf{r})\frac{\partial T(\mathbf{r},t)}{\partial t} = \nabla\cdot(k(\mathbf{r})\nabla T(\mathbf{r},t)) + S(\mathbf{r}) + A^*(\mathbf{r},T)$$
$$- B^*(\mathbf{r},T)(T^*(\mathbf{r},t) - T_B(T)), \tag{1}$$

where the notation is as follows (parameters that are affected by the thermoregulatory system are denoted with star signs (*)):

C: specific heat of the tissue [J kg^{-1} K^{-1}]

T: instantaneous temperature of the tissue [K]

ρ: mass density of the tissue [kg m^{-3}]

k: thermal conductivity of the tissue [W m^{-1} K^{-1}]

S: electromagnetic power absorption in the tissue [W m^{-3}]

A^*: metabolic heat generation of the tissue [W m^{-3}]. Respiratory heat loss in the lungs and evaporative losses on the skin may also be included in A^*, if they are not taken into account in the boundary conditions. Metabolic heat generation may be affected by the temperature increase.

B^*: blood perfusion rate through the tissue [J kg^{-1} K^{-1}]. By the Pennes bioheat equation, the rate of heat transfer between the blood and tissue is proportional to the product of the perfusion rate B^* and the difference of the arterial and tissue temperature $T - T_B^*$. The blood perfusion B^* may be separated into

$$B = \omega_B^* \rho_B C_B (1 - \kappa), \tag{2}$$

where C_B is the specific heat of blood [J kg^{-1} K^{-1}], ρ_B is the density of blood [kg m^{-3}], and ω_B^* is the volumetric perfusion rate [m^3 kg^{-1} s^{-1}]. Factor κ accounts for the incomplete thermal equilibrium between the blood and tissue. Pennes and most subsequent studies have set $\kappa = 0$. The blood flow value in the skin is highly dependent on the thermoregulatory controller.

T_B^*: temperature of the arterial blood (body core temperature) [K]. To maintain thermal balance, the blood temperature T_B^* must satisfy

$$\rho_B V_B \frac{\partial T_B}{\partial t} = \int B(T - T_B)\,\mathrm{d}V. \tag{3}$$

The left hand side of (3) is the time derivative of the total thermal energy of blood, and the right side is the total heat transferred between the blood and other tissues. The temperature of the arterial blood is assumed to be constant, both spatially and temporally, in the original Pennes model.

41

On the skin-air surface, there is a boundary condition with the form of the Newton cooling law

$$-k(\mathbf{r})\frac{\partial T(\mathbf{r},t)}{\partial n} = H(\mathbf{r})(T(\mathbf{r},t)-T_E)+E_S^*(\mathbf{r},T). \qquad (4)$$

The left side of (4) is the outward heat flux, and the right side denotes its components. The first term on the right hand side combines the convective, conductive and radiative heat loss, with the heat transfer coefficient H and the environment temperature T_E. The second term E_S^*, which is highly dependent on the thermoregulation, denotes the heat loss due to the evaporation on the skin.

The Pennes (1948) heat transfer model has been criticised for various reasons (Arkin *et al* 1994, Wissler 1998), but nevertheless, the bioheat equation has generally yielded results that agree with experimental observations. There is a lack of noninvasive experimental means for measuring deep tissue temperatures, which limits the progress in developing more realistic models (Wissler 1998). Several alternative models for accounting the blood perfusion have been developed, but they generally lack a sound experimental grounding (Arkin *et al* 1994). An alternative to the bioheat approach, the discrete vascularized thermal diffusion model (DIVA, Kotte *et al* 1996) has seen increasing use in several recent studies of the RF exposure, the main advantage of the DIVA model being the ability to take into account the individual blood vessels. However, there are no experimental data to support the model. Even recently, the lack of noninvasive means for measuring the internal temperature distribution is still a problem in, for example, hyperthermia treatment (Paulides *et al* 2010).

3.1.1 Simplified bioheat equation

The bioheat equation (1) can be made simpler by making several assumptions. The blood temperature T_B may be assumed to be temporally constant for localized RF heating scenarios, because the human thermoregulatory system attempts to maintain thermal homoeostasis. The thermoregulatory response may be ignored, which results in a linear equation that is much easier to solve, and which yields overestimation of the temperature rise. Additionally, in a thermal steady-state, the time derivatives may be set to zeros, which gives overestimation of the time-dependent temperature rise. More terms may be removed from the equation by investigating only the temperature rise $\delta T = T - T_0$, where T_0 is the basal temperature without the electromagnetic power absorption term S. Studying only the steady-state temperature rise cancels out C, ρ, A, T_B, E_S, and T_E. The resulting simple equation, which was used in paper (IV), reads

$$(\nabla\cdot k\nabla - B)\delta T + S = 0, \qquad (5)$$

with boundary condition

$$\left(k\frac{\partial}{\partial n} + H\right)\delta T = 0, \tag{6}$$

where k is the thermal conductivity, B is the blood perfusion rate, S is the electromagnetic power absorption, and H is the combined heat transfer coefficient to air, including the convective, conductive and radiative heat loss.

Equation (5) may only be used for estimating the localized temperature rises. It is insufficient for modelling the body-core temperature rise, because it is assumed that the blood temperature does not increase during the exposure, i.e., the heat transferred to blood just disappears. For the local temperature values, ignoring the blood temperature increase is a good approximation if the total power absorption is much smaller than the basal metabolic heat generation (about 100 W for a male adult), which is true for most localized exposure sources. Because the thermoregulatory function is effective in reducing the blood temperature rise, the blood temperature rise is much smaller than the local peak temperature rises even for the whole body plane-wave exposure (Bernardi *et al* 2003, Hirata *et al* 2007a). Also, when studying sufficiently short exposures, the use of (5) is well justified even for the whole-body exposure because the thermal time constants for the blood temperature are much longer than those for the local peak temperatures: Typically the temperature will rise to the steady state by an exponential approach, with the thermal time constant for the body core temperature rise about 22–52 min (whole-body SAR 0.4 W kg^{-1}) depending on the sweating rate (Hirata *et al* 2007a, 2008a), and 6–8 min for the local peak temperatures (Leeuwen *et al* 1999, Wang and Fujiwara 1999, Bernardi *et al* 2000).

Taking the blood temperature rise into account would cause the temperature values throughout the body to increase somewhat: The whole-body averaged SAR at the basic restriction limit for the occupational exposure (0.4 W kg^{-1} by ICNIRP (1998a)) causes a blood temperature increase in the range of 0.10–0.25 °C, depending on the sweating rate and on the ratio of the skin surface area to the body mass (Hirata *et al* 2007a, 2008a). The blood temperature increase is particularly significant for the tissues located deep inside the body or in the areas which are not directly irradiated (Hirata *et al* 2007a). For example, the temperature rise in the foetus, which is quite well protected against high SAR values, is caused mainly by the temperature elevation of the maternal blood (Kikuchi *et al* 2010).

Hirata *et al* (2007a) and Kikuchi *et al* (2010) compared the non-steady-state version of the simplified bioheat equation (5) to the complete bioheat equation (1) with the thermoregulation (Section 3.1.2) and the blood temperature rise (3). The locations and magnitudes of the peak temperatures seemed to match reasonably well between the simplified and complete models, but, as discussed above, the temperature rises in the non-directly exposed tissues were considerably higher with the complete model. It might be that the differences in the peak temperatures between the two models are smaller than
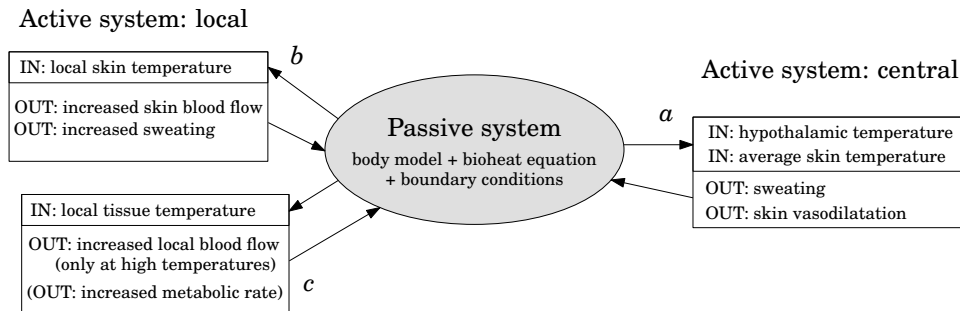
Figure 8: Simplified diagram of the thermoregulatory system. Boxes *a–c* list the most important responses to the central and localized temperature increases.

the variations caused by, for instance, the uncertainty and regional variation in the skin blood perfusion rates (Section 3.1.3). Hence, the simplified bioheat equation (1) is a fairly good approximation of the complete model, but only when studying the peak temperature increases.

3.1.2 Thermoregulatory models

Human thermal models are often defined in terms of the *passive* and *active* systems. The passive system refers to the thermal system defined by the bioheat equation (1) and the boundary conditions, while the active system consists of the physiological control functions which send/receive feedback to/from the passive system (Figure 8). Early human passive thermal models were based on simplified shapes, such as cylinders and spheres (Wissler 2009). Recently, anatomically realistic body models have been used, which has allowed accurate modelling of localized temperature increases. Passively, the human body loses heat by radiation, conduction, convection and evaporation (4). Actively, the main mechanisms by which the body attempts to increase the heat dissipation are increases in the skin blood flow by vasodilatation, and sweating with consequent evaporative heat loss. These mechanisms are defined by the controller signals which depend on the hypothalamic temperature and the average skin temperature, as analyzed in the influential theoretical study by Stolwijk and Hardy (1966). The computer model (Stolwijk 1971), which evolved from the Stolwijk and Hardy (1966) model, has been the basis for many later numerical models of the active thermal system. Recent studies with anatomically realistic whole-body models (Bernardi *et al* 2003, Hirata *et al* 2007a, 2008a, Kikuchi *et al* 2010) have adopted a model mainly similar to the Stolwijk (1971) model, with additions and modifications from several sources (Chatterjee and Gandhi 1983, Spiegel 1984, Hoque and Gandhi 1988, Fiala *et al* 2001).

Models of human thermoregulation have been originally developed and

validated for the human body subjected to different environmental conditions or levels of exercise (Stolwijk and Hardy 1966, Spiegel 1984, Wissler 2009). So one must ask if the same models are applicable to absorption of the RF radiation, which represents a unique form of heat loading in which the tissue temperatures increase in an individual without the application of infrared radiation, exposure to increased ambient temperature, fever, or exercise. Adair and Black (2003) conducted an extensive review of the thermal responses to the RF energy absorption, and it was concluded that the normal human thermoregulatory system functions very effectively against the heat load due to the RF energy absorption, even at levels high above the exposure guidelines. The thermoregulatory responses to the excessive RF energy absorption seem to be no different from the responses to other forms of external/internal heat load (Adair and Black 2003), so there is a reason to believe that the mathematical models of the thermoregulatory system are suited also for the analysis of the RF heating.

Vasodilatation, i.e., an increase in the blood perfusion of the skin, and sweating are triggered by the temperature rise in the thermosensors on the skin or in the hypothalamus (Stolwijk and Hardy 1966), illustrated in Figure 8 by box *a*. In addition, the elevation in local skin temperature decreases the flow resistance of cutaneous veins, further increasing the skin blood flow (Stolwijk 1971) (Figure 8, box *b*). These mechanisms boost the heat dissipation into the environment by increasing the convective heat transfer by blood between the body core and the skin, and by increasing the evaporative heat loss on the skin surface. For any external heat stress factors, the temperature rise in the hypothalamus is caused by the rise in the blood temperature. For the RF heating, because the hypothalamus is located deep inside head, the effect of the local SAR on the temperature rise in the hypothalamus is small for the localized exposure of the head (Wang and Fujiwara 1999), and for the whole-body plane-wave exposure both at the resonance frequency and in the GHz range (Hirata *et al* 2007a). Hence it seems that the hypothalamic temperature rise is caused mainly by the increased blood temperature in the case of the RF heating, too. Earlier, it had been suggested that focused RF heating solely in the hypothalamus—a highly unlikely scenario in reality (Wang and Fujiwara 1999, Hirata *et al* 2007a)—could trigger the thermoregulatory response even excess of that needed to dissipate the heat, causing a fall in the overall body temperature (Stolwijk 1980, Spiegel 1984).

In addition to the skin blood flow increase, it has been observed that the blood flow in internal tissues is increased greatly as the tissue temperatures are increased from 39 °C to 45 °C (Stolwijk 1980)(Figure 8, box *c*). This kind of response makes it more difficult to raise only the local tissue temperatures because the heat is transferred effectively into the other parts of the body. Several recent computational studies (Bernardi *et al* 2003, Hirata *et al* 2007a, 2008a, Kikuchi *et al* 2010) have modelled the local increase of blood flow in internal tissues by employing the model proposed by Chatterjee and

Gandhi (1983). However, the original authors note that the knowledge is limited, and that the model should be tested further. Some tests were performed by Hirata *et al* (2006b) who applied the Chatterjee and Gandhi (1983) blood flow model to the RF heating of rabbits, and compared the simulated temperatures to measurements in rabbit eyes. Different assumptions for the blood flow rate variation with the increase of the temperature were tested, and the model with the original parameters yielded the best match with the measured temperature rises. However, it is still unclear how well the model is applicable to human beings or other parts of the body.

3.1.3 Uncertainty in thermal models

There are several uncertainty factors in computational modelling of the temperature. Of course, the temperature values are affected by uncertainty of the calculated power-loss (Section 2) that is used as an input parameter. However, the bioheat equation always gives a smoother temperature solution than the source data, so the temperature is insensitive to small variations in the EM power-loss distribution. Much of the uncertainty in temparature values is related to the modelling of the skin which is by far the most important organ in the human thermoregulation. Overall, the greatest problem in the human thermal modelling might be the biological variability of individuals (Wissler 2009). For example, laboratory studies of RF heating during magnetic resonance (MR) imaging have reported a poor correlation between the body or skin temperature changes versus the whole-body averaged SAR values during MR procedures. Therefore, the thermal reactions to a given SAR may be quite variable depending on the individual's thermoregulatory system (Shellock 2000, Shellock and Crues 2004).

Widely-used basal blood perfusion rate B values of various tissues were derived by Williams and Leggett (1989), who compiled the results from a large number of studies and determined the blood flow values from the average cardiac output to each organ. It is noteworthy that the uncertainty of the blood flow value *inter alia* in the skin was very high, and the reference value for the skin blood flow was 'assigned arbitrarily'. The skin blood perfusion value which apparently originates from the arbitrary reference value by Williams and Leggett (1989) has been used in many recent studies, for example in Wainwright (2000), Bernardi *et al* (2003), Buccella *et al* (2007), Hirata *et al* (2007c), and paper (IV), to name a few. The skin blood is also highly dependent on the thermoregulatory controller and there are individual and regional differences in the sweat gland distribution and vasodilatation. In addition, the blood flow and metabolic rates in the skeletal muscles and skin are highly affected by different levels of exercise.

The skin blood perfusion rate varies considerably between different regions of the body (Stolwijk 1971, Gordon *et al* 1976), but no recent thermal calculations of the RF exposure have taken this variation into account. Ac-

tually, the reference value for the skin blood perfusion (Williams and Leggett 1989) has been derived by using a different blood perfusion rate for the specific regions of the body. Intuitively, the assumption of a constant blood perfusion over the whole skin is a reasonable simplification when studying the body core temperature rise during the whole-body exposure. But the same may not be true for the localized exposure, especially in the head. Namely, the blood perfusion in the cephalic skin is considerably higher than the average, for instance, B in the facial skin may be about 10 times larger than in the thorax/abdomen (Gordon *et al* 1976). An example of the effect of the blood perfusion may be found in the study by Hirata *et al* (2007c), who investigated several uncertainty factors affecting the temperature rise in the eyes. The skin blood perfusion rate of 9100 J $(\text{s K m}^3)^{-1}$ (the same as in Williams and Leggett 1989) was compared to 40000 J $(\text{s K m}^3)^{-1}$ (blood perfusion rate of the facial skin in Gordon *et al* (1976) is about 45000 J $(\text{s K m}^3)^{-1}$). Using the higher value resulted in about a 20 % decrease in the eye lens temperature. It was observed that the blood perfusion rate of the skin might be the most significant single factor affecting the temperature rise.

Thermal conductivity values k have had a much smaller relative variation between different tissues compared to the variations of, for example, the dielectric properties or the blood perfusion rates. Hence, the possible uncertainty in the thermal conductivity has much a smaller impact on the temperature rise and thermal diffusion length than the uncertainty in the blood perfusion rate (Hirata *et al* 2006a).

Using anatomical voxel models instead of the early simplified cylindrical and spherical thermal models have allowed realistic modelling of the localized temperature rises. However, the transition from the simplified models to voxel models has brought about some new modelling problems. Modern anatomical voxel models with cell sizes greater than or equal to 2 mm typically overestimate the volume of the skin (Nagaoka *et al* 2004, Dimbylow 2005a), which may be corrected by treating the outer skin layer as a composite tissue of skin and subcutaneous fat. Also, unlike the simplified models, the voxel models are unable to directly take into account the regional differences in skin thickness (Anderson *et al* 2010). These factors bring even more uncertainty for the thermal properties of the skin.

Another drawback of using the voxel models compared to the simplified models is the staircase approximation which causes overestimation of the skin-air surface area (Samaras *et al* 2006). The overestimated surface area increases the heat dissipation into the surrounding air, which results in an underestimation of the temperature rise. A scheme to remove this staircasing error by tuning the heat transfer coefficient H in (6) has been proposed by Neufeld *et al* (2007), and a simpler approximation of it has been employed in paper (IV), where it was also shown that the staircase correction only had a marginal impact on the temperature rise. This is in line with the results by Wang and Fujiwara (1999), who reported relatively small changes in the
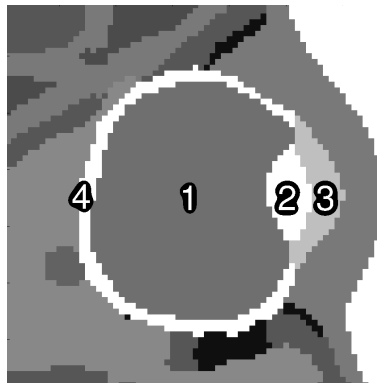
Figure 9: Transverse slice of the 0.5 mm voxelized eye of the Virtual family male model (Christ *et al* 2010b). The model only contains four eye tissues: vitreous body (1), lens (2), cornea (3), and sclera (4). The cornea tissue also contains the anterior and posterior chambers and iris, and the sclera tissue contains the choroid and retina.

temperature values in the head with different values for H.

3.1.4 RF heating of the eye

The eye (Snell and Lemp 1998) is one of the most sensitive organs to thermal damage. Animal studies have shown that heating due to the absorption of the RF energy in the eyes may cause various ocular effects, such as irreversible changes in the lens (cataracts) and also effects on the cornea and retina (Elder 2003). Limiting the temperature elevation in the eyes has been used as the basis for the basic restrictions on the localized RF exposure (ICNIRP 1998a, IEEE 2005). The threshold temperature increase for the cataract is roughly 5–7 °C in rabbit eyes, requiring high doses of microwave energy (Guy *et al* 1975). Non-human primate studies have shown that the RF heating that would cause cataractogenesis in the lens would also produce unacceptable effects (burns) in other parts of the eye and face (Elder 2003). There is also evidence that a long term exposure to smaller SARs does not cause ocular effects (Elder 2003).

The eyeball features several thin sheet-like tissue structures with high contrasts in both the blood perfusion and metabolic rates. Several eye tissues such as the cornea, lens and vitreous humour are avascular, i.e., there is no blood perfusion. The posterior outer layer of the eyeball consists of thin sheets of the retina with a high metabolic rate (thickness 0.1-0.6 mm), the highly vascularized choroid (0.1-0.2 mm), and the relatively avascular sclera (0.3-1.0 mm). Because of the high retinal and choroidal blood flow, the eyeball has been modelled by applying convective boundary conditions on the sclera (Lagendijk 1982), but that model is unable to take into account the heat gen-

48

erated outside the eyeball and conducted into the eye (Hirata 2005). It has been shown that the conducted heat may be as large as the heat generated inside the eyeball (Wainwright 2007). Recently, the temperature rise in the eyes has been simulated by using voxel models of the whole head. Because of the limited resolution of the voxel models, most eye models only consist of a few tissues which should be treated as composite tissues with averaged material parameters (Figure 9). As the bioheat equation has a thermal diffusion length in the order of a few centimetres (Hirata *et al* 2006a), omitting small details using the composite tissue model may still provide good results. The sensitivity of the temperature rise to the composite value of the scleral blood flow has been studied by several authors (Wainwright 2007, Hirata *et al* 2007c). Buccella *et al* (2007) calculated temperature rise in the eye by using separate sclera and choroid/retina models with various blood perfusion rates. After compensating several other uncertainty factors (Hirata *et al* 2007c), the results were in good agreement with other studies. Discrete vascularized thermal diffusion model (DIVA, Kotte *et al* 1996) has been shown to give fairly good agreement with the bioheat equation for the RF heating of the eye (Flyckt *et al* 2006, 2007).

According to paper (IV), the maximum 10-g cubically-averaged SAR in the eye of 1 W kg^{-1} causes a temperature elevation of about 0.1–0.15 °C in the lens in the frequency range from 1 to 10 GHz, which agrees also with the other computational studies. The thermoregulatory response was not modelled in paper (IV), nor in any of the above studies. Hence, for high power levels capable of causing harmful effects, the ratio between the temperature and SAR will actually be perhaps considerably smaller. Rabbit studies have shown good agreement between the measured and simulated temperature elevations in rabbit eyes (Hirata *et al* 2006b, 2008b). However, as the human thermoregulatory system and facial structure are greatly different from rabbits, it remains uncertain how well the simulated values for humans correspond to reality.

3.2 Solving bioheat equation using the multigrid method

In paper (IV), the geometric multigrid method was used to solve the bioheat equation (5) numerically. Details of the solution method, which were omitted for brevity in that paper, are described in this section.

When a cubical grid with constant cell size h is employed, equation (5) can be discretized as

$$\frac{1}{h^2}\left\{\sum_{j\in\mathcal{N}_i\cap\mathscr{I}^h}\left[\frac{2k_ik_j}{k_i+k_j}(T_j-T_i)\right]+\sum_{j\in\mathcal{N}_i\setminus\mathscr{I}^h}K_iT_i\right\}-B_iT_i=-S_i,\qquad i\in\mathscr{I}^h,\ (7)$$

where $\mathscr{I}^h$ denotes the set of the non-air cells inside the body and $\mathcal{N}_i$ is the set of the six neighbouring cells of cell i. The second sum term in the equation
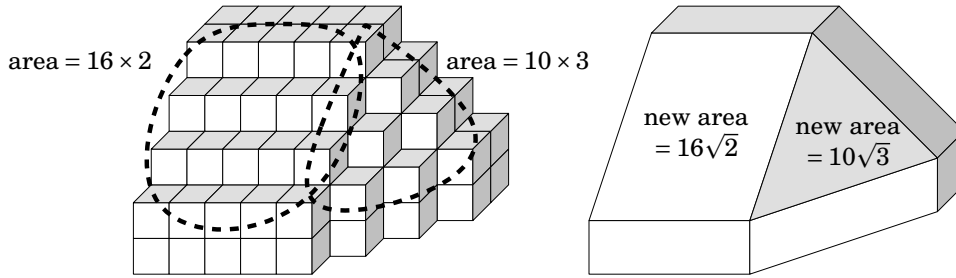
Figure 10: Correction of the staircasing error using the method of paper (IV). The left figure shows the staircased model without correction, and the right figure shows the effective areas after correction.

takes the boundary condition (6) into account by a linear approximation when

$$K_i = \frac{-2k_i h H_i}{2k_i + h H_i},$$

which is derived from the boundary condition in Neufeld *et al* (2007). In paper (IV), the heat transfer coefficient H_i was scaled downwards by dividing it with $\sqrt{N}$, where N is the number of cells in $\mathcal{N}_i \setminus \mathcal{I}$, i.e., the number of neighbouring air cells of the cell i. This was done to reduce the overestimation of the skin-air surface area caused by the staircase approximation of curved boundaries (Samaras *et al* 2006, Neufeld *et al* 2007). For example, if the number of neighbouring air cells were 2, the heat transfer would be divided by $\sqrt{2}$. Figure 10 shows an example on how the scheme reduces the effective surface area.

Equation (7) is effectively a linear equation system of the form

$$\mathbf{A}^h \mathbf{u}^h = \mathbf{b}^h, \tag{8}$$

which could be solved by whatever method. In paper (IV), the multigrid method with the Gauss-Seidel iteration was used. During the iteration, the actual matrix $\mathbf{A}^h$ was never constructed, but the coefficients were calculated on the fly from the grid and material parameters k, B and H. The advantages of the multigrid method are the small memory requirements, fast convergence and relatively easy implementation.

First, coarse grids $\mathcal{I}^{2h}$, $\mathcal{I}^{4h}$, etc. and the corresponding material parameters are constructed. The coarse grids use the same kind of difference equation as (7). Material parameters of the coarse grids were arithmetic averages of the material parameters of the finest grid in paper (IV). After the coarse geometries have been constructed, the flow of the multigrid algorithm is roughly the following:

1. Choose an initial guess for $\mathbf{u}^h$

2. Do n steps of Gauss-Seidel iteration

3. Calculate the residual
$$\mathbf{r}^h = \mathbf{b}^h - \mathbf{A}^h \mathbf{u}^h$$
and restrict $\mathbf{r}^h$ to the coarse grid $\mathscr{I}^{2h}$. The restriction operation from fine grid to coarse grid used in paper (IV) was the arithmetic averaging.

4. Using the coarse grid, solve the error correction $\mathbf{e}^{2h}$ by the multigrid (recursion) from
$$\mathbf{A}^{2h} \mathbf{e}^{2h} = \mathbf{r}^{2h}.$$
This results in an recursive algorithm, where only the coarsest grid is solved directly. However, the implementation of the solver in paper (IV) was done without recursion.

5. Prolongate $\mathbf{e}^{2h}$ to the fine grid $\mathscr{I}^h$, and make the correction
$$\mathbf{u}^h \leftarrow \mathbf{u}^h + \mathbf{e}^h.$$
The prolongation operation from the coarse grid to fine grid was the linear interpolation in paper (IV).

6. Do m steps of the Gauss-Seidel iteration, and get the approximation $\mathbf{u}^h$.

This procedure is repeated until the residual norm is sufficiently small. One round of this kind of iteration is called a V-cycle. In the solver used in paper (IV), the V-cycle consisted of 7 levels, with the resolution halved for each level, i.e., for the 0.5 mm voxel model, the resolution of the coarsest grid was 32 mm. The numbers of Gauss-Seidel iterations at each step were $n = 4$ and $m = 1$.

The above procedure is the most basic multigrid algorithm, but it was sufficient for the studied problem. The performance could have been made better by several ways, including: the more general SOR iteration could have been used instead of the Gauss-Seidel iteration, solutions for the coarse grids could have been used as the initial guesses for the finer grids (the full multigrid method), or the code could have been parallelized. However, as the convergence was fast enough and the problem was not very hard, no further tuning was done. The finest resolution that was used was 0.5 mm which is probably more than sufficient for thermal calculations. It can be concluded that the computational requirements are small even for the largest reasonable thermal simulations of the absorption of microwave energy, and that the multigrid method seems to be very well suited for these kinds of simulations.

4 Summary of publications

(I) *Performance of convolutional PML absorbing boundary conditions in finite-difference time-domain SAR calculations*

The performance of convolutional perfectly-matched layer (CPML) absorbing boundary conditions (ABCs) is studied for the specific absorption rate (SAR) calculations. The subject is important because the design of the ABCs plays a key role in the accuracy and memory consumption of FDTD simulations. Earlier, the effect of ABCs have been studied in Wang *et al* (2006a), where it was concluded that for maintaining a reasonable accuracy, the absorbing boundary should be placed relatively far away from the studied object, i.e., a large amount of empty space needed to be included between the boundary and the studied human body model. This would mean a large increase in the computational burden of FDTD simulations for SAR calculations. However, later Findlay and Dimbylow (2006a) showed that for their computational code, the error due to the PML absorbing boundary was small, and the boundary could be placed very close to the studied human body model. This paper not only confirms the results of Findlay and Dimbylow (2006a), but also presents cases where the standard PML might be insufficient. The performance of CPML ABCs for various parameter configurations is studied by varying the distance from the exposed object to the absorbing boundary and comparing the SAR values for each distance. Several different geometries are considered, including canonical objects such as a small muscle sphere or a box, as well as an anatomically realistic human body model. Plane waves and short dipoles at frequencies from 100 MHz to 5 GHz are used as the exposure sources. The main conclusion is that the computational error due to a properly implemented and tuned CPML ABC is negligibly small no matter how close the absorbing boundary is positioned from the studied object.

(II) *Alternative approach for modeling material interfaces in FDTD*

This paper presents a simple alternative way for including lossy dielectric materials in the FDTD grid. The standard 'E-cell' and the proposed 'H-cell' methods are presented. The main contribution of this paper are the interesting results about the performance of the two methods. Firstly, the FDTD field solutions of the plane-wave exposure of a lossy dielectric sphere are studied for a varying sphere radius. The material parameters of the sphere match those of the '2/3 muscle', that is, a weighted average of the parameters of the muscle (2/3) and fat (1/3) tissues. When the frequency is kept constant and the sphere radius is varied, there are spherical (TE^r and TM^r) resonances at certain radii. The performance of the proposed methods is particularly interesting

near these resonance frequencies. The E-cell method gives a very good agreement with the analytic Mie-series solutions near the lowest TE^r resonance even when using low resolutions. However, it produces a relatively large error near the lowest TM^r resonance even for high resolutions. On the contrary, the performance of the H-cell method is very good near the TM^r resonance, and not so good near the TE^r resonance. Further tests are calculated for a layered lossy dielectric sphere for various frequencies. Again, it seems that for some frequencies, the H-cell method is clearly the better choice, while the E-cell method is better for some other frequencies. These results suggest that generally the standard E-cell method and the proposed H-cell method perform equally well, and which method is better for a particular problem depends on the actual field solution.

(III) *The effect of finite-difference time-domain resolution and power-loss computation method on SAR values in plane-wave exposure of Zubal phantom*

In this paper, the E- and H-cell methods are applied for the simulations of the plane-wave exposure of the Zubal phantom. Four different algorithms for calculating the SAR values are utilised. Both the whole-body-averaged and 10 g-averaged SAR are calculated using two different FDTD cell sizes, 1.8 mm and 3.6 mm. Based on the results it seems that the SAR values in a realistic exposure case may be affected moderately by the choice between the E- and H-cells and by the power-loss calculation algorithm. Because of this, it might be necessary to state accurately how the power loss should be calculated when developing the computational standards for dosimetry.

(IV) *Assessment of computational uncertainty of temperature rise and SAR in the eyes and brain under far-field exposure from 1 to 10 GHz*

This paper deals with the SAR and temperature rise in the head due to the exposure to plane waves in a wide frequency range from 1 to 10 GHz. A particular focus is on the relationships between the computational uncertainty, frequency and resolution of the computational model. Two anatomically realistic head models, male and female, are used, and the temperature rise and SAR in the eyes and brain are computed. The FDTD method with the CPML absorbing boundary conditions is employed for solving the electromagnetic problem. The corresponding thermal problem is modelled by the bioheat equation, which is solved by the geometric multigrid method. The computational uncertainty with respect to the frequency and cell resolution is assessed by first computing the SAR and temperature-rise values for a very fine resolution of 0.5 mm, and then comparing the results of the same calculations repeated with the lower resolutions of 1 mm and 2 mm. The

results suggest that the 2 mm resolution should only be used for the frequencies smaller than 2.5 GHz, and the 1 mm resolution only for frequencies under 5 GHz. The morphological differences in models seem to be an important cause of variation: Differences in the results between the two different head models are usually larger than the computational error due to the grid resolution, and larger than the difference between the results for the open and closed eyes. Limiting the incident plane-wave power density to less than $100 \, \mathrm{W \, m^{-2}}$ is sufficient to ensure that the temperature rise in the eyes and brain is less than $1 \, ^\circ\mathrm{C}$ in the whole frequency range.

(V) *SAR variation study from 300 to 5000 MHz for 15 voxel models including different postures*

This paper presents an extensive study on the specific absorption rate (SAR) covering 720 simulations using the FDTD method. High resolution whole-body models are irradiated with plane waves from 300 MHz to 5 GHz by applying various incoming directions and polarizations. The total number of whole-body models is 15, consisting of seven heterogeneous models, two homogenized versions of the heterogeneous models, and one homogeneous model in six different postures. The weight of the body models ranges from 18 to 105 kg. Detailed results of the variation of both the whole-body averaged SAR and peak $10 \, \mathrm{g}$ SAR with incident direction, polarization, body model, and posture are reported. The findings state, for example, that for an adult, the effect of the incoming direction on the whole-body SAR is larger in the GHz range than at around 300–450 MHz, and the effect is stronger with vertical polarization. Also, the body posture has little effect on the whole-body averaged SAR in the GHz range, but at around 300–450 MHz, one may even expect a 50 % rise in the whole-body SAR if the posture is changed from the standing position. The effect of the posture on the peak $10 \, \mathrm{g}$ SAR is much larger than on the whole-body averaged SAR. The polarization of the incident electric field may have an effect of tens of percents on the whole-body SAR. In the GHz range, the horizontal polarization gives higher whole-body SAR values compared to the vertical polarization, especially for the irradiation from the lateral direction. A comparison between homogeneous and heterogeneous models was performed, and it seemed that the homogenized models do not generally produce a conservative estimate for the whole-body SAR compared to the original heterogeneous models, except at the highest 5 GHz frequency. The basic restriction of the whole-body SAR, set by ICNIRP, is exceeded in the smallest models (~20 kg) at the reference level of exposure, but also some adult phantoms are close to the limit. The peak $10 \, \mathrm{g}$ SAR limits are never exceeded in the studied cases.

54

(VI) *Comparison of SAR calculation algorithms for finite-difference time-domain method*

The FDTD method produces an electric field which is located on the edges of the Yee cells, and it is not immediately clear how the field should be interpreted when determining the SAR values in each cell. Significantly varying SAR values may result from the use of different algorithms for determining the SAR. In this paper, the divergence of SAR values due to different SAR calculation algorithms are studied, and it is examined if some SAR calculation algorithm should be preferred over others. For this purpose, numerical FDTD results are compared to analytical solutions in a one-dimensional layered model and a three-dimensional spherical object. Additionally, the dataset of paper (V), consisting of a large number of SAR simulations, is exploited to study the implications of the SAR calculation algorithms for the dosimetry of anatomically realistic whole-body models. The results show that the trapezium algorithm—based on the trapezium integration rule—is always conservative compared to the analytic solution, making it a good choice for worst-case exposure assessment. On the contrary, the mid-ordinate algorithm—named after the mid-ordinate integration rule—usually underestimates the analytic SAR. The linear algorithm—which is approximately a weighted average of the two—seems to be the most accurate choice overall, typically giving the best fit with the shape of the analytic SAR distribution. For anatomically realistic models, the whole-body SAR difference between different algorithms is relatively independent of the used body model, incident direction and polarization of the plane wave. The main factors affecting the difference are cell size and frequency.

(VII) *Computational estimation of magnetically induced electric fields in a rotating head*

This paper is about the human exposure to extremely low-frequency electromagnetic fields. Unlike the other papers, this paper does not deal with the RF electromagnetic fields, so the FDTD method is not used. A slowly changing magnetic field or movement in a static magnetic field may induce electric fields in human tissues, which could potentially cause harmful effects. However, currently there are no confirmed biological hazards, and effects are limited to short-term sensory reactions. These include magnetic-field induced vertigo and phosphenes, which are thought to be caused by stimulation by the induced electric currents in the vestibular system or retinas, respectively. In this paper, the electric currents induced by extremely low frequency magnetic fields are computed. This gives information for approximating the threshold electric field values of phosphenes and magnetic-field-

55

induced vertigo effects. The computed results are also compared to the basic restriction limits set by IEEE and ICNIRP in order to estimate the compliance of the different rotational head movements in a strong static magnetic field, for example, near MRI scanners. For these purposes, the induced electric field is solved using the finite-element method (FEM). Various rotational movements for four different head models are studied, but because of the quasi-static approach, the results are also applicable to, for instance, 20 Hz frequencies. Under the rotational movement of the head, with a magnetic flux rate of change of 1 T s^{-1}, the maximum IEEE-averaged electric field and maximum ICNIRP-averaged current density were 337 mV m^{-1} and 8.84 mA m^{-2}, respectively. The limits set by IEEE seem to be significantly stricter than those by ICNIRP. The results show that a magnetic flux rate of change of 1 T s^{-1} may induce an electric field in the range of 50 mV m^{-1} near the retinas, and possibly even larger values near the inner ears. These results provide information for approximating the threshold electric field values of phosphenes and vertigo-like effects.

References

Ackerman M J 1998 The Visible Human Project *Proc. IEEE* **86** 504–11

Adair E R and Black D R 2003 Thermoregulatory responses to RF energy absorption *Bioelec-tromagnetics* **24**(S6) S17–38

Anderson V, Croft R, and McIntosh R L 2010 SAR versus S_{inc}: What is the appropriate RF exposure metric in the range 1-10 GHz? Part I: Using planar body models *Bioelectromag-netics* **31**(6) 454–66

Arkin H, Xu L, and Holmes K 1994 Recent developments in modeling heat transfer in blood perfused tissues *IEEE Trans. Biomed. Eng.* **41**(2) 97 –107

Bakker J F, Paulides M M, Christ A, Kuster N, and van Rhoon G C 2010 Assessment of induced SAR in children exposed to electromagnetic plane waves between 10 MHz and 5.6 GHz *Phys. Med. Biol.* **55**(11) 3115–30

Beard B and Kainz W 2004 Review and standardization of cell phone exposure calculations using the SAM phantom and anatomically correct head models *BioMedical Engineering OnLine* **3**(1) 34

Beard B B, Kainz W, Onishi T, Iyama T, Watanabe S, Fujiwara O, Wang J, Bit-Babik G, Faraone A, Wiart J, Christ A, Kuster N, Lee A K, Kroeze H, Siegbahn M, Keshvari J, Abrishamkar H, Simon W, Manteuffel D, and Nikoloski N 2006 Comparisons of computed mobile phone induced SAR in the SAM phantom to that in anatomically correct models of the human head *IEEE Trans. Electromagn. Compat.* **48**(2) 397–407

Bérenger J P 1994 A perfectly matched layer for the absorption of electromagnetic waves *J. Comput. Phys.* **114** 185–200

Bérenger J P 2002 Numerical reflection from FDTD-PMLs: A comparison of the split PML with the unsplit and CFS PMLs *IEEE Trans. Antennas Propag.* **50** 258–65

Bernardi P, Cavagnaro M, Pisa S, and Piuzzi E 2000 Specific absorption rate and temperature increases in the head of a cellular-phone user *IEEE Trans. Microw. Theory Tech.* **48**(7) 1118–26

Bernardi P, Cavagnaro M, Pisa S, and Piuzzi E 2003 Specific absorption rate and temperature elevation in a subject exposed in the far-field of radio-frequency sources operating in the 10-900-MHz range *IEEE Trans. Biomed. Eng.* **50**(3) 295–304

Buccella C, De Santis V, and Feliziani M 2007 Prediction of temperature increase in human eyes due to RF sources *IEEE Trans. Electromagn. Compat.* **49**(4) 825–33

Caputa K, Okoniewski M, and Stuchly M A 1999 An algorithm for computations of the power deposition in human tissue *IEEE Antennas Propag. Mag.* **41** 102–7

Cassola V F, de Melo Lima V J, Kramer R, and Khoury H J 2010 FASH and MASH: female and male adult human phantoms based on polygon mesh surfaces: I. development of the anatomy *Phys. Med. Biol.* **55**(1) 133–62

Chatterjee I and Gandhi O P 1983 An inhomogeneous thermal block model of man for the electromagnetic environment *IEEE Trans. Biomed. Eng.* **BME-30**(11) 707 –15

Christ A and Kuster N 2005 Differences in RF energy absorption in the heads of adults and children *Bioelectromagnetics* **26**(S7) S31–44

Christ A, Klingenböck A, Samaras T, Goiceanu C, and Kuster N 2006 The dependence of electromagnetic far-field absorption on body tissue composition in the frequency range from 300 MHz to 6 GHz *IEEE Trans. Microw. Theory Tech.* **54**(5) 2188–95

Christ A, Gosselin M C, Christopoulou M, Kühn S, and Kuster N 2010a Age-dependent tissue-specific exposure of cell phone users *Phys. Med. Biol.* **55**(7) 1767–83

Christ A, Kainz W, Hahn E G, Honegger K, Zefferer M, Neufeld E, Rascher W, Janka R, Bautz W, Chen J, Kiefer B, Schmitt P, Hollenbach H P, Shen J, Oberle M, Szczerba D, Kam A, Guag J W, and Kuster N 2010b The Virtual Family—development of surface-based anatomical models of two adults and two children for dosimetric simulations *Phys. Med. Biol.* **55**(2) N23–38

Conil E, Hadjem A, Lacroux F, Wong M F, and Wiart J 2008 Variability analysis of SAR from 20 MHz to 2.4 GHz for different adult and child models using finite-difference time-domain *Phys. Med. Biol.* **53**(6) 1511–25

Dimbylow P 2005a Resonance behaviour of whole-body averaged specific energy absorption rate (SAR) in the female voxel model, NAOMI *Phys. Med. Biol.* **50**(17) 4053–63

Dimbylow P 2005b Development of the female voxel phantom, NAOMI, and its application to calculations of induced current densities and electric fields from applied low frequency magnetic and electric fields *Phys. Med. Biol.* **50**(6) 1047–70

Dimbylow P and Bolch W 2007 Whole-body-averaged SAR from 50 MHz to 4 GHz in the University of Florida child voxel phantoms *Phys. Med. Biol.* **52**(22) 6639–49

Dimbylow P, Bolch W, and Lee C 2010 SAR calculations from 20 MHz to 6 GHz in the University of Florida newborn voxel phantom and their implications for dosimetry *Phys. Med. Biol.* **55**(5) 1519–30

Dimbylow P J 1997 FDTD calculations of the whole-body averaged SAR in an anatomically realistic voxel model of the human body from 1 MHz to 1 GHz *Phys. Med. Biol.* **42** 479–90

Dimbylow P J 2002 Fine resolution calculations of SAR in the human body for frequencies up to 3 GHz *Phys. Med. Biol.* **47**(16) 2835–46

Dimbylow P J, Hirata A, and Nagaoka T 2008 Intercomparison of whole-body averaged SAR in European and Japanese voxel phantoms *Phys. Med. Biol.* **53**(20) 5883–97

Dimbylow P J, Nagaoka T, and Xu X G 2009 A comparison of foetal SAR in three sets of pregnant female models *Phys. Med. Biol.* **54**(9) 2755–67

Drossos A, Santomaa V, and Kuster N 2000 The dependence of electromagnetic energy absorption upon human head tissue composition in the frequency range of 300-3000 MHz *IEEE Trans. Microw. Theory Tech.* **48**(11) 1988–95

Elder J 2003 Ocular effects of radiofrequency energy *Bioelectromagnetics* **24**(S6) S148–61

Fiala D, Lomas K J, and Stohrer M 2001 Computer prediction of human thermoregulatory and temperature responses to a wide range of environmental conditions *Int. J. Biometeorol.* **45**(3) 143–59

Findlay R P and Dimbylow P J 2005 Effects of posture on FDTD calculations of specific absorption rate in a voxel model of the human body *Phys. Med. Biol.* **50**(16) 3825–35

Findlay R P and Dimbylow P J 2006a Variations in calculated SAR with distance to the perfectly matched layer boundary for a human voxel model *Phys. Med. Biol.* **51** N411–5

Findlay R P and Dimbylow P J 2006b FDTD calculations of specific energy absorption rate in a seated voxel model of the human body from 10 MHz to 3 GHz *Phys. Med. Biol.* **51**(9) 2339–52

Flyckt V M M, Raaymakers B W, and Lagendijk J J W 2006 Modelling the impact of blood flow on the temperature distribution in the human eye and the orbit: fixed heat transfer coefficients versus the pennes bioheat model versus discrete blood vessels *Phys. Med. Biol.* **51**(19) 5007–21

Flyckt V M M, Raaymakers B W, Kroeze H, and Lagendijk J J W 2007 Calculation of SAR and temperature rise in a high-resolution vascularized model of the human eye and orbit when exposed to a dipole antenna at 900, 1500 and 1800 MHz *Phys. Med. Biol.* **52**(10) 2691–701

Gabriel C 2005 Dielectric properties of biological tissue: Variation with age *Bioelectromagnetics* **26**(S7) S12–8

Gabriel C and Peyman A 2006 Dielectric measurement: error analysis and assessment of uncertainty *Phys. Med. Biol.* **51**(23) 6033–46

Gabriel C, Gabriel S, and Corthout E 1996a The dielectric properties of biological tissues: I. Literature survey *Phys. Med. Biol.* **41**(11) 2231–49

Gabriel S, Lau R W, and Gabriel C 1996b The dielectric properties of biological tissues: II. Measurements in the frequency range 10 Hz to 20 GHz *Phys. Med. Biol.* **41**(11) 2251–69

Gabriel S, Lau R W, and Gabriel C 1996c The dielectric properties of biological tissues: III. Parametric models for the dielectric spectrum of tissues *Phys. Med. Biol.* **41**(11) 2271–93

Gedney S D 1996 An anisotropic perfectly matched layer absorbing medium for truncation of FDTD lattices *IEEE Trans. Antennas Propag.* **44** 1630–9

Gordon R G, Roemer R B, and Horvath S M 1976 A mathematical model of the human temperature regulatory system - transient cold exposure response *IEEE Trans. Biomed. Eng.* **BME-23**(6) 434–44

Gosselin M C, Christ A, Kühn S, and Kuster N 2009 Dependence of the occupational exposure to mobile phone base stations on the properties of the antenna and the human body *IEEE Trans. Electromagn. Compat.* **51**(2) 227–35

Guy A W, Lin J C, Kramar P O, and Emery A F 1975 Effect of 2450-MHz radiation on the rabbit eye *IEEE Trans. Microw. Theory. Techn.* **MTT-23**(6) 492–8

Habachi A E, Conil E, Hadjem A, Vazquez E, Wong M F, Gati A, Fleury G, and Wiart J 2010 Statistical analysis of whole-body absorption depending on anatomical human characteristics at a frequency of 2.1 GHz *Phys. Med. Biol.* **55**(7) 1875–87

Hand J, Li Y, Thomas E, Rutherford M, , and Hajnal J 2006 Prediction of specific absorption rate in mother and fetus associated with MRI examinations during pregnancy *Magnetic Resonance in Medicine* **55** 883–93

Hand J W 2008 Modelling the interaction of electromagnetic fields (10 MHz-10 GHz) with the human body: methods and applications *Phys. Med. Biol.* **53**(16) R243–86

Hand J W, Li Y, and Hajnal J V 2010 Numerical study of RF exposure and the resulting temperature rise in the foetus during a magnetic resonance procedure *Phys. Med. Biol.* **55** (4) 913–30

59

Hirata A 2005 Temperature increase in human eyes due to near-field and far-field exposures at 900 MHz, 1.5 GHz, and 1.9 GHz *IEEE Trans. Electromagn. Compat.* **47**(1) 68–76

Hirata A and Fujiwara O 2009 The correlation between mass-averaged SAR and temperature elevation in the human head model exposed to RF near-fields from 1 to 6 GHz *Phys. Med. Biol.* **54**(23) 7227–38

Hirata A, Fujimoto M, Asano T, Wang J, Fujiwara O, and Shiozawa T 2006a Correlation between maximum temperature increase and peak SAR with different average schemes and masses *IEEE Trans. Electromagn. Compat.* **48**(3) 569–78

Hirata A, Watanabe S, Kojima M, Hata I, Wake K, Taki M, Sasaki K, Fujiwara O, and Shiozawa T 2006b Computational verification of anesthesia effect on temperature variations in rabbit eyes exposed to 2.45 GHz microwave energy *Bioelectromagnetics* **27** 602–12

Hirata A, Asano T, and Fujiwara O 2007a FDTD analysis of human body-core temperature elevation due to RF far-field energy prescribed in the ICNIRP guidelines. *Phys. Med. Biol.* **52**(16) 5013–23

Hirata A, Kodera S, Wang J, and Fujiwara O 2007b Dominant factors influencing whole-body average SAR due to far-field exposure in whole-body resonance frequency and GHz regions *Bioelectromagnetics* **28**(6) 484–7

Hirata A, Watanabe S, Fujiwara O, Kojima M, Sasaki K, and Shiozawa T 2007c Temperature elevation in the eye of anatomically based human head models for plane-wave exposures *Phys. Med. Biol.* **52**(21) 6389–99

Hirata A, Asano T, and Fujiwara O 2008a FDTD analysis of body-core temperature elevation in children and adults for whole-body exposure *Phys. Med. Biol.* **53**(18) 5223–38

Hirata A, Sugiyama H, Kojima M, Kawai H, Yamashiro Y, Fujiwara O, Watanabe S, and Sasaki K 2008b Computational model for calculating body-core temperature elevation in rabbits due to whole-body exposure at 2.45 GHz *Phys. Med. Biol.* **53**(12) 3391–404

Hirata A, Ito N, and Fujiwara O 2009 Influence of electromagnetic polarization on the whole-body averaged SAR in children for plane-wave exposures *Phys. Med. Biol.* **54**(4) N59–65

Hirata A, Fujiwara O, Nagaoka T, and Watanabe S 2010 Estimation of whole-body average SAR in human models due to plane-wave exposure at resonance frequency *IEEE Trans. Electromagn. Compat.* **52**(1) 41–8

Holland R 1993 Pitfalls of staircase meshing *IEEE Trans. Electromagn. Compat.* **35**(4) 434–9

Hoque M and Gandhi O 1988 Temperature distributions in the human leg for VLF-VHF exposures at the ANSI-recommended safety levels *IEEE Trans. Biomed. Eng.* **35**(6) 442 –9

ICNIRP 1998a Guidelines for limiting exposure to time-varying electric, magnetic and electromagnetic fields (up to 300 GHz) *Health Phys.* **74**(4) 492–522

ICNIRP 1998b Response to questions and comments on ICNIRP EMF guidelines *Health Phys.* **75**(4) 438–9

ICNIRP 2009 *Review of the scientific evidence on dosimetry, biological effects, epidemiological observations, and health consequences concerning exposure to high frequency electromagnetic fields (100 kHz to 300 GHz).* International Commission on Non-Ionizing Radiation Protection Oberschleißheim, Germany

IEEE 2002 *IEEE Recommended Practice for Measurements and Computations of Radio Frequency Electromagnetic Fields With Respect to Human Exposure to Such Fields, 100 kHz-300 GHz, C95.3-2002* Institute of Electrical and Electronics Engineers New York doi: 10.1109/IEEESTD.2002.94226

IEEE 2005 *IEEE Standard for Safety Levels with Respect to Human Exposure to Radio Frequency Electromagnetic Fields, 3 kHz to 300 GHz, C95.1-2005* Institute of Electrical and Electronics Engineers New York doi: 10.1109/IEEESTD.2006.99501

Ilvonen S, Toivonen T, Toivo T, Uusitupa T, and Laakso I 2008 Numerical specific absorption rate analysis and measurement of a small indoor base station antenna *Microw. Opt. Techn. Let.* **50**(10) 2516–21

Joseph W and Martens L 2005 Comparison of safety distances based on the electromagnetic field and based on the SAR for occupational exposure of a 900-MHz base station antenna *IEEE Trans. Electromagn. Compat.* **47**(4) 977–85

Kainz W, Christ A, Kellom T, Seidman S, Nikoloski N, Beard B, and Kuster N 2005 Dosimetric comparison of the specific anthropomorphic mannequin (SAM) to 14 anatomical head models using a novel definition for the mobile phone positioning *Phys. Med. Biol.* **50**(14) 3423–45

Kawai H, Nagaoka T, Watanabe S, Saito K, Takahashi M, and Ito K 2010 Computational dosimetry in embryos exposed to electromagnetic plane waves over the frequency range of 10 MHz–1.5 GHz *Phys. Med. Biol.* **55**(1) N1–11

Keshvari J and Lang S 2005 Comparison of radio frequency energy absorption in ear and eye region of children and adults at 900, 1800 and 2450 MHz *Phys. Med. Biol.* **50**(18) 4355–69

Keshvari J, Keshvari R, and Lang S 2006 The effect of increase in dielectric values on specific absorption rate (SAR) in eye and head tissues following 900, 1800 and 2450 MHz radio frequency (RF) exposure *Phys. Med. Biol.* **51**(6) 1463–77

Kikuchi S, Saito K, Takahashi M, and Ito K 2010 Temperature elevation in the fetus from electromagnetic exposure during magnetic resonance imaging *Phys. Med. Biol.* **55**(8) 2411–25

Kim C H, Choi S H, Jeong J H, Lee C, and Chung M S 2008 HDRK-Man: a whole-body voxel model based on high-resolution color slice images of a Korean adult male cadaver *Phys. Med. Biol.* **53**(15) 4093–106

Kotte A, van Leeuwen G, de Bree J, van der Koijk J, Crezee H, and Lagendijk J 1996 A description of discrete vessel segments in thermal modelling of tissues *Phys. Med. Biol.* **41** (5) 865–84

Kühn S, Jennings W, Christ A, and Kuster N 2009 Assessment of induced radio-frequency electromagnetic fields in various anatomical human body models *Phys. Med. Biol.* **54**(4) 875–90

Laakso I 2007 FDTD method in assessment of human exposure to base-station radiation Master's thesis Helsinki University of Technology

Laakso I and Uusitupa T Edge- or face-based electric field in FDTD: Implications for dosimetry In *2010 Asia-Pacific Radio Science Conference (AP-RASC'10), Toyama, Japan, September 22-26* 2010

Lacroux F, Conil E, Cortel Carrasco A, Gati A, Wong M F, and Wiart J 2008 Specific absorption rate assessment near a base-station antenna (2.140 MHz): some key points *Annals of Telecommunications* **63**(1) 55–64

Lagendijk J J W 1982 A mathematical model to calculate temperature distributions in human and rabbit eyes during hyperthermic treatment *Phys. Med. Biol.* **27**(11) 1301–11

Lazzi G, Gandhi O, and Sullivan D 2000 Use of PML absorbing layers for the truncation of the head model in cellular telephone simulations *IEEE Trans. Microw. Theory Tech.* **48**(11) 2033–9

Leeuwen G M V, Lagendijk J J, Leersum B J V, Zwamborn A P, Hornsleth S N, and Kotte A N 1999 Calculation of change in brain temperatures due to exposure to a mobile phone *Phys. Med. Biol.* **44**(10) 2367–79

Lin J C and Bernardi P 2007 *Bioengineering and Biophysical Aspects of Electromagnetic Fields* chapter Computational methods for predicting field intensity and temperature change, pages 293–380 CRC Press (Boca Raton, FL) 3rd, illustrated edition

Martínez-Búrdalo M, Martín A, Anguiano M, and Villar R 2005 On the safety assessment of human exposure in the proximity of cellular communications base-station antennas at 900, 1800 and 2170 MHz *Phys. Med. Biol.* **50** 4125–37

Mason P A, Hurt W D, Walters T J, D'Andrea J A, Gajsek P, Ryan K L, Nelson D A, Smith K I, and Ziriax J M 2000 Effects of frequency, permittivity, and voxel size on predicted specific absorption rate values in biological tissue during electromagnetic-field exposure *IEEE Trans. Microw. Theory Tech.* **48** 2050–8

McIntosh R L and Anderson V 2010 SAR versus S_{inc}: What is the appropriate RF exposure metric in the range 1-10 GHz? Part II: Using complex human body models *Bioelectromagnetics* **31**(6) 467–78

Nagaoka T and Watanabe S 2008 Postured voxel-based human models for electromagnetic dosimetry *Phys. Med. Biol.* **53**(24) 7047–61

Nagaoka T and Watanabe S 2009 Voxel-based variable posture models of human anatomy *Proc. IEEE* **97**(12) 2015–25

Nagaoka T, Watanabe S, Sakurai K, Kunieda E, Watanabe S, Taki M, and Yamanaka Y 2004 Development of realistic high-resolution whole-body voxel models of Japanese adult males and females of average height and weight, and application of models to radio-frequency electromagnetic-field dosimetry *Phys. Med. Biol.* **49**(1) 1–15

Nagaoka T, Togashi T, Saito K, Takahashi M, Ito K, and Watanabe S 2007 An anatomically realistic whole-body pregnant-woman model and specific absorption rates for pregnant-woman exposure to electromagnetic plane waves from 10 MHz to 2 GHz *Phys. Med. Biol.* **52**(22) 6731–45

Nagaoka T, Kunieda E, and Watanabe S 2008 Proportion-corrected scaled voxel models for Japanese children and their application to the numerical dosimetry of specific absorption rate for frequencies from 30 MHz to 3 GHz *Phys. Med. Biol.* **53**(23) 6695–711

Neufeld E, Chavannes N, Samaras T, and Kuster N 2007 Novel conformal technique to reduce staircasing artifacts at material boundaries for FDTD modeling of the bioheat equation *Phys. Med. Biol.* **52**(15) 4371–81

Paulides M M, Bakker J F, Linthorst M, van der Zee J, Rijnen Z, Neufeld E, Pattynama P M T, Jansen P P, Levendag P C, and van Rhoon G C 2010 The clinical feasibility of deep hyperthermia treatment in the head and neck: new challenges for positioning and temperature measurement *Phys. Med. Biol.* **55**(9) 2465–80

Pennes H H 1948 Analysis of tissue and arterial blood temperature in the resting human forearm *J. Appl. Physiol.* **1**(2) 93–122

Peyman A, Rezazadeh A A, and Gabriel C 2001 Changes in the dielectric properties of rat tissue as a function of age at microwave frequencies *Phys. Med. Biol.* **46** 1617–29

Peyman A, Gabriel C, Grant E H, Vermeeren G, and Martens L 2009 Variation of the dielectric properties of tissues with age: the effect on the values of SAR in children when exposed to walkie-talkie devices *Phys. Med. Biol.* **54**(2) 227–41

Roden J A and Gedney S D 2000 Convolution PML (CPML): An efficient FDTD implementation of the CFS-PML for arbitrary media *Microw. Opt. Techn. Let.* **27**(5) 334–9

Sacks Z S, Kingsland D M, Lee R, and Lee J F 1995 A perfectly matched anisotropic absorber for use as an absorbing boundary condition *IEEE Trans. Antennas Propag.* **43** 1460–3

Samaras T, Christ A, and Kuster N 2006 Effects of geometry discretization aspects on the numerical solution of the bioheat transfer equation with the FDTD technique *Phys. Med. Biol.* **51**(11) N221–9

Shellock F G 2000 Radiofrequency energy-induced heating during MR procedures: A review *Journal of Magnetic Resonance Imaging* **12** 30–6

Shellock F G and Crues J V 2004 MR procedures: Biologic effects, safety, and patient care *Radiology* **232** 635–52

Snell R S and Lemp M A 1998 *Clinical anatomy of the eye* Wiley-Blackwell (Abingdon, England) 2nd edition

Spiegel R J 1984 A review of numerical models for predicting the energy deposition and resultant thermal response of humans exposed to electromagnetic fields *IEEE Trans. Microw. Theory Tech.* **MTT-32**(8) 730–46

Spitzer V M and Whitlock D G 1998 The visible human dataset: The anatomical platform for human simulation *Anat. Rec.* **253**(2) 49–57

Stolwijk J A J 1971 *A mathematical model of physiological temperature regulation in man* NASA Contractor Rep. NASA Cr-1855 New Haven, Connecticut

Stolwijk J A J 1980 Mathematical models of thermal regulation *Annals of the New York Academy of Sciences* **335** (Thermal Characteristics of Tumors Applications in Detection and Treatment) 98–106

Stolwijk J A J and Hardy J D 1966 Temperature regulation in man—a theoretical study *Pflügers Archiv European Journal of Physiology* **291**(2) 129–62

Taflove A and Hagness S C 2005 *Computational Electrodynamics: The Finite-Difference Time-Domain Method* Artech House (Boston, MA) 3rd edition

Thors B, Strydom M, Hansson B, Meyer F, Kärkkäinen K, Zollman P, Ilvonen S, and Tornevik C 2008 On the estimation of SAR and compliance distance related to RF exposure from mobile communication base station antennas *IEEE Trans. Electromagn. Compat.* **50**(4) 837–48

Thors B, Hansson B, and Törnevik C 2009 The generation of simple compliance boundaries for mobile communication base station antennas using formulae for SAR estimation *Phys. Med. Biol.* **54**(13) 4243–56

Van de Kamer J B, Kroeze H, De Leeuw A A C, and Lagendijk J J W 2001 Quasistatic zooming of FDTD E -field computations: the impact of down-scaling techniques *Phys. Med. Biol.* **46**(5) 1539–51

Wainwright P 2000 Thermal effects of radiation from cellular telephones *Phys. Med. Biol.* **45**(8) 2363–72

Wainwright P R 2007 Computational modelling of temperature rises in the eye in the near field of radiofrequency sources at 380, 900 and 1800 MHz *Phys. Med. Biol.* **52**(12) 3335–50

Wang J and Fujiwara O 1999 FDTD computation of temperature rise in the human head for portable telephones *IEEE Trans. Microw. Theory Tech.* **47**(8) 1528–34

Wang J, Fujiwara O, Kodera S, and Watanabe S 2006a FDTD calculation of whole-body average SAR in adult and child models for frequencies from 30 MHz to 3 GHz *Phys. Med. Biol.* **51** 4119–27

Wang J, Fujiwara O, and Watanabe S 2006b Approximation of aging effect on dielectric tissue properties for SAR assessment of mobile telephones *IEEE Trans. Electromagn. Compat.* **48**(2) 408–13

Wiart J, Hadjem A, Wong M F, and Bloch I 2008 Analysis of RF exposure in the head tissues of children and adults *Phys. Med. Biol.* **53**(13) 3681–95

Williams L R and Leggett R W 1989 Reference values for resting blood flow to organs of man *Clin. Phys. Physiol. Meas.* **10**(3) 187–217

Wissler E H 1998 Pennes' 1948 paper revisited *J. Appl. Physiol.* **85**(1) 35–41

Wissler E H 2009 *Advances in Numerical Heat Transfer* chapter Whole-body human thermal models, pages 257–306 CRC Press (Boca Raton, FL) illustrated edition

Yee K S 1966 Numerical solution of initial boundary value problems involving Maxwell's equations in isotropic media *IEEE Trans. Antennas Propag.* **14** 302–7

Zaidi H and Tsui B 2009 Review of computational anthropomorphic anatomical and physiological models *Proc. IEEE* **97**(12) 1938–53

Zubal I, Harrell C, Smith E, Rattner Z, Gindi G, and Hoffer P 1994 Computerized three-dimensional segmented human anatomy *Medical Phys.* **21(2)** 299–302

Errata

It is mentioned in paper (I) that the value for $\alpha_{\max}$ should be inversely proportional to the size of the problem (Bérenger 2002). This fact is important and requires some clarification. The approximate optimum value given by Bérenger (2002) is

$$\alpha_0 = \frac{c\epsilon}{w}, \tag{9}$$

where c and ϵ are the speed of light and permittivity in the medium, and w is the size of the simulated structure. For the small muscle sphere and the small muscle box in paper (I), $\alpha_{\max}$ calculated by (9) is close to the $\alpha = 0.05$ used in that paper. For the whole-body Norman model studied in paper (I), $\alpha_{\max} = 0.05$ is too large. However, this does not show because the frequencies are sufficiently high. For lower frequencies, for instance, about 70 MHz, too large $\alpha_{\max}$ would result in a significant reflection and erroneous results. Small optimum $\alpha_{\max}$ is also the reason why the regular PML performs so well for whole-body models (Findlay and Dimbylow 2006a).

BUSINESS +
ECONOMY

ART +
DESIGN +
ARCHITECTURE

SCIENCE +
TECHNOLOGY

CROSSOVER

DOCTORAL
DISSERTATIONS